Physics of Plasmas

Blob wakes in NSTX

Cite as: Phys. Plasmas **26**, 072502 (2019); https://doi.org/10.1063/1.5094872
Submitted: 06 March 2019 . Accepted: 11 June 2019 . Published Online: 17 July 2019

S. J. Zweben, J. R. Myra, A. Diallo, D. A. Russell, F. Scotti, and D. P. Stotler

Physics of Plasmas ARTICLE scitation.org/journal/php

Blob wakes in NSTX

Cite as: Phys. Plasmas **26**, 072502 (2019); doi: 10.1063/1.5094872
Submitted: 6 March 2019 · Accepted: 11 June 2019 ·
Published Online: 17 July 2019

S. J. Zweben,[1] J. R. Myra,[2] A. Diallo,[1] D. A. Russell,[2] F. Scotti,[3] and D. P. Stotler[1]

AFFILIATIONS

[1]Princeton Plasma Physics Laboratory, Princeton, New Jersey 08540, USA
[2]Lodestar Research Corporation, Boulder, Colorado 80301, USA
[3]Lawrence Livermore National Laboratory, Livermore, California 94550, USA

ABSTRACT

Transient small-scale structures were identified in the wake of blobs moving poloidally through the scrape-off layer of high-powered H-mode plasmas in NSTX, using the gas puff imaging (GPI) diagnostic. These blob wakes had a poloidal wavelength in the range of $\lambda_{pol} = 3.5 \pm 0.7$ cm, which is significantly smaller than the average blob scale of $L_{pol} \sim 12$ cm, and the wakes had a poloidal velocity of $V_{pol} = 1.5 \pm 1.0$ km/s in the electron diamagnetic direction, which is opposite to the blob poloidal velocity in these shots. These wakes were radially localized 0–4 cm outside the separatrix and occurred within ~50 μs after the passage of a blob through the GPI field of view. The clearest wakes were seen when the GPI viewing angle was well aligned with the local B field line, as expected for such small-scale structures given the diagnostic geometry. A plausible theoretical interpretation of the wakes is discussed: the observed wakes share some features of drift waves and/or drift-Alfvén waves which could be excited by the blobs.

I. INTRODUCTION

A. Background

Edge fluctuations in tokamaks are normally either totally random (i.e., turbulent), periodically bursting (e.g., edge localized modes or ELMs), or continuous and quasicoherent. Very rarely are these fluctuations observed to spontaneously grow from an initially stable state (e.g., Ref. 1), since their growth rate is typically microseconds, while the time scale for tokamak pulses is typically hundreds of milliseconds. Therefore, it is difficult to study the physics of most edge fluctuations since they rapidly evolve into a complicated nonlinear regime.

In this paper, we describe initial observations of "blob wakes," which exhibit a regular pattern which is neither random, periodically bursting, nor quasicoherent, and so present an interesting new aspect of tokamak edge stability. Blob wakes are triggered by the passage of a blob and are observed to grow transiently and locally in the scrape-off layer (SOL) just after the passage of a blob. The blobs which cause these wakes are high density SOL structures (a.k.a. intermittent objects or edge filaments) which were first described by a relatively simple theory[2] and then studied experimentally in DIII-D,[3] NSTX,[4] and other tokamaks.[5] Blobs are important since they have been found to cause about half of the turbulent cross-field transport in the SOL of tokamaks.[5] Measurements of blobs are continuing on tokamaks such as MAST,[6] ASDEX Upgrade,[7] and TCV,[8] as well as in stellarators.[9] As far as we know, until now, there has been no previous mention of blob wakes in either the experimental or theoretical literature.

The goal of this paper is to provide an initial description and discussion of blob wakes for a selected set of high-power H-mode plasmas in NSTX, based on data from the gas puff imaging (GPI) diagnostic. The blobs discussed in this paper mainly move poloidally in the SOL, as usual for H-mode plasmas in NSTX.[4] The main motivation is curiosity-driven, since it is surprising that such wakes occur at all in this normally random dataset. Their relatively simple structure and motion may make it possible to understand the physics of their growth, which could also help clarify the physics of blobs in tokamaks. However, since these wakes are relatively rare and localized in space and time, they probably do not contribute significantly to edge transport, which is the most practical consequence of edge fluctuations.

The GPI diagnostic and the database for this paper are discussed in Secs. I B and I C, and the experimental results from NSTX are described in Sec. II. Section III contains some additional discussion, including theoretical interpretations and potential improvements to help understand these measurements.

B. GPI diagnostic

The gas puff imaging (GPI) diagnostic on NSTX was described most recently in Ref. 10, and generic GPI diagnostic issues were discussed in a recent review.[11] The data used in this paper were taken during the last run year of NSTX (2010).

The NSTX GPI diagnostic viewed a region just above the outer midplane near the separatrix through a Dα line filter using a fast

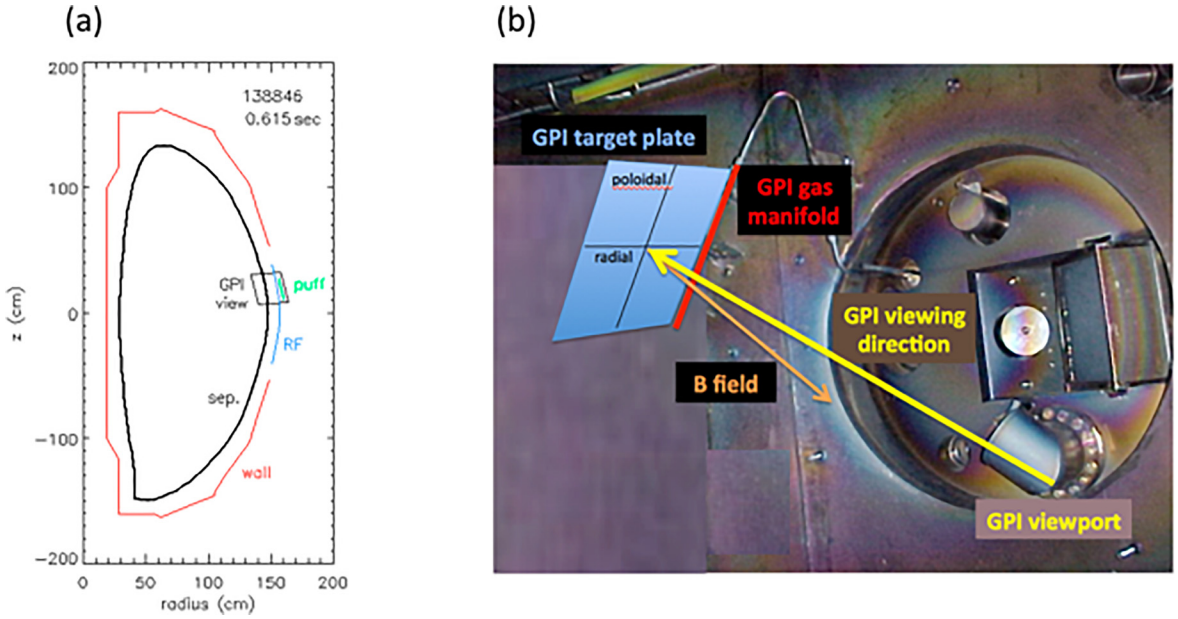

FIG. 1. GPI geometry in NSTX. (a) is a cross section of a typical NSTX plasma in the radial vs vertical plane (R, z), showing the trapezoidal GPI field of view just above the outer midplane and the GPI gas puff manifold as a green line. (b) is a photo of the GPI hardware inside the vessel, with the GPI gas puff manifold attached to the outer wall ~20 cm above the outer midplane. The GPI optical view is shown by the yellow arrow with the optical vertex at the right, with a B field line shown schematically in orange, and with the optical calibration target plate highlighted in blue (attached to the manifold). Reproduced with permission from Zweben *et al.*, Phys. Plasmas **24**, 102509 (2017). Copyright 2017 AIP Publishing.

camera at 398 000 frames/s. This view was approximately along the local magnetic field line direction, as illustrated in Fig. 1 (taken from Ref. 10), and covered ~24 cm radially by ~30 cm poloidally (i.e., in the binormal direction), with an optical spatial resolution of ~0.5 cm. A pulsed deuterium gas puff was used to increase the local light emission for an ~50 ms period during the steady state part of the discharge. The GPI geometry localizes the light emitting region to a radial vs poloidal plane perpendicular to the local magnetic field, although the finite parallel size of the gas cloud introduces some spatial smearing of field-aligned filaments due to slight misalignments of the GPI view with the local B field,[10] which is important in the resolution of small-scale structures such as wakes.

The general issue of the interpretation of GPI data is discussed in detail in Ref. 11. The measured fluctuations in the Dα light emission can be due to electron density, electron temperature, or possibly neutral density fluctuations. For the presentation and analysis of the data in Sec. II, we make no assumption about the underlying cause of these fluctuations and so analyze only the measured 2D light emission patterns in space and time.

C. Database

The 12 NSTX shots used for this paper are listed in Table I. All shots were high-power H-mode plasmas with high field (B = 5.0–5.5 kG), high current (I = 0.9–1.1 MA), and near-maximum NBI (neutral beam injection) power (P = 6 MW). The magnetic geometry was a lower-single-null divertor shape and similar for all cases. These shots came from an experiment to study ion-scale modes at the top of the H-mode pedestal.[12] There were ELMs during these shots, but not at the times of the clear blob wakes.

All shots which had GPI data during this experiment are shown in Table I. The GPI gas puff strength was the same for all and the same as Refs. 4 and 10, with the resulting Dα light emission rate peaking at ~412 ms for the first 9 shots and ~512 ms for the last three shots (due to later gas puff triggering). Both puffs occurred during the steady-state phases of these discharges, since the plasma current and NBI were constant during 0.3–0.6 s. This paper focuses on GPI data within ±5 ms of these peak times when the GPI signal was the largest.

TABLE I. Shot list (time of the peak GPI signal).

Shot	Time (ms)	Ip (MA)	Bt (kG)	NBI (MW)	Rsep (cm)
139 044	412	1.0	4.9	6.0	147.2
139 045	412	1.0	4.9	6.0	147.6
139 047	412	1.0	4.9	6.0	147.3
139 048	412	1.1	5.4	6.0	146.4
139 049	412	1.1	5.4	6.0	146.9
139 050	412	1.1	5.4	6.0	147.4
139 053	412	1.1	5.4	6.0	147.6
139 054	412	1.1	5.4	6.0	147.9
139 056	412	0.91	5.4	6.0	147.6
139 057	512	0.91	5.4	6.0	147.6
139 058	512	1.0	4.9	6.0	147.4
139 059	512	1.0	4.9	6.0	147.1

However, similar blob wakes were seen in the GPI data at other times during these shots and in many other shots in the larger 2010 GPI database,[13] including those at lower NBI power and B field.

Even within the shot and time constraints of Table I, this GPI dataset contains hundreds of examples of blobs and blob wakes. Only some of the clearest examples are used for illustration in Secs. II A–II E, while a statistical analysis of blob wakes is described in Secs. II F–II H.

II. BLOB WAKE RESULTS

The basic observations and identification of blob wakes are illustrated with selected examples in Secs. II A–II E. Automated wake analysis is described in Sec. II F, and analysis results from the complete database are discussed in Sec. II G.

A. Image sequences

Figure 2(a) shows a set of 24 sequential frames of raw GPI camera data from one of the shots in Table I (#139 053), covering a total of ∼60 μs during the steady-state portion of the discharge starting at 414.616 ms. The frame sequence is from upper left to lower right, and the time between frames is 2.5 μs. The Dα light intensity is displayed in a linear false-color red scale with zero offset, and each image covers 24 cm radially (i.e., horizontal) × 30 cm poloidally (i.e., vertical). A high brightness blob enters this region from the top of frame #1 (upper left) and then moves downward (poloidally) by ∼6 cm through frame #6 (upper right), i.e., at a speed of ∼5 km/s in the ion diamagnetic drift direction. During this short time, the blob location remains just outside the separatrix (thick dashed line) with a roughly constant shape and size.

The blob wake starts to form just above the blob in frames #4–7 in Fig. 2(a) and lasts until about frame #18, i.e., ∼30 μs. During this time, the wakes appear to peel off one-at-a-time from the top edge of the blob as it moves downward, and finally a near-periodic wake is formed behind the blob in the poloidal direction. For example, in frame #14, there appear to be ∼5 clear maxima in the blob wake over a vertical distance of ∼12 cm, i.e., with a wake wavelength of ∼4 cm. After frame #17, both the wake and the blob seem to disappear, and a new blob appears to be forming just above the vertical center of the frame by frame #22.

Another example from a different shot (#138 048) is shown in Fig. 2(b). Here, the blob again enters the frame at the top (frame #1) and starts to move poloidally downward just outside the separatrix. In this case, the blob wake starts to form at about frame #5 and lasts until about frame #21 (i.e., for ∼40 μs). The wakes in frame #18 show a near-periodic poloidal structure with a wavelength of ∼3–4 cm near the vertical center of the image. These wakes seem to dissipate or become randomized after about frame #22. The poloidally varying tilt of these wakes (e.g., in frame #18) is discussed in Sec. II C.

A video showing blob wakes in the shots of Table I is available on a web site[14] and in the supplementary material of this paper. All shots show some wakes after blobs, but not all blobs have wakes, and some of the shots show wakes more frequently and clearly than others.

B. Spatial filtering

A simple method to help identify the spatial structure of these blob wakes is illustrated in Fig. 3 for a single frame from shot #139 053. Part (a) shows the raw GPI data taken when the wakes are as clear as possible, i.e., from Fig. 2(a) at frame #14. The thick dashed vertical line indicates the vertical column of pixels in which the wakes will be evaluated (i.e., column i = 31 of the 64 horizontal pixels in the image), and the thin dashed line is the separatrix (from EFIT02). In part (b), the raw data signal is plotted vs the poloidal (i.e., vertical) distance at column i = 31. There are four clear peaks in the signal over the poloidal range 7.5–22.5 cm of the 30 cm high image (i.e., rows j = 20–60 of the 80 pixels in the image) and similar peaks in adjacent columns within about ±1 cm. In this case, the standard deviation of the amplitude of the signal at i = 31 over this range is ∼24% of the mean. The time-averaged raw data signal in this column is shown by the dashed line in Fig. 3(b) and is peaked near the vertical center due to the poloidally localized gas puff and optical vignetting.

The image in Fig. 3(c) is the same frame as in Fig. 3(a) but smoothed (boxcar averaged) over 7 pixels (2.6 cm) in both the horizontal and vertical directions (without any time smoothing). Figure 3(d) is an image of the raw data minus the smoothed data, i.e., after this high-pass spatial filtering intended to highlight the structures below ∼6 cm in wavelength. This color map uses red/white to show positive regions and blue/black to show negative regions, with green near zero. The blue edge region to the right of the wakes is caused by subtracting the smoothed image, which extends slightly outward from the radial location of the raw data (this is not relevant for the analysis at i = 31 below). The wake maxima are not perfectly aligned vertically, and so some of the wake structure is missed in any single column. The wake maxima near the vertical centerline in this frame are ∼2.5–3.0 cm outside this separatrix (which is itself is uncertain by about 1–2 cm). The dashed horizontal lines are separated by 5 cm poloidally.

Figure 4 shows a group of single frames, one from each of the 12 shots in this database, all spatially high-pass filtered as in Fig. 3(d). These frames were chosen to illustrate some of the clearest wake structures within ±5 ms of the time of the peak GPI signal in each shot. In every case, these wakes are preceded by blobs moving downward just outside the separatrix; for example, these blobs can be seen as the white (highest signal) regions below the wake structures in shots #139 044, #139 045, #139 049, and #139 058. The columns where the wake modulations are the largest are indicated by the thick dashed vertical lines (used for analysis below), and separatrices are shown by the thin dashed lines. Horizontal dashed lines separated by 5 cm poloidally are shown for reference.

Blob wake structures appear as a poloidal (i.e., vertical) modulation in every shot in Fig. 4 but also display a significant variation in their radial and poloidal location, modulation intensity, and periodicity. Since they are also transient (as shown in Fig. 2), the wakes are not easy to identify automatically with a simple algorithm. But roughly speaking, the poloidal wavelength of the blob wakes is ∼3–4 cm, their strongest modulation is located ∼0–4 cm outside the separatrix, and their apparent radial width is ∼2–3 cm in the SOL region. Note that the observable radial width of the wakes is partially limited by the radial width of the GPI emission region, which is typically ∼5 cm (FWHM) or ∼10 cm (full-width) at the vertical center of these images and radially centered near the separatrix in these high-power H-mode shots. Due to this spatial limitation and also the optical misalignment effect discussed just below, the radial structure of the wakes will not be emphasized in this paper.

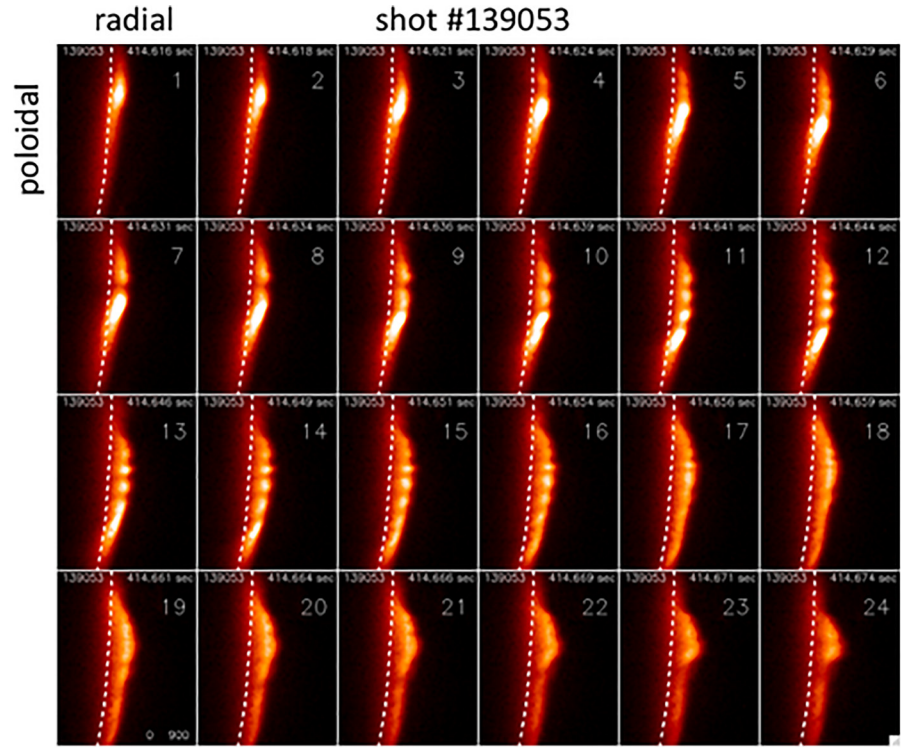

(a)

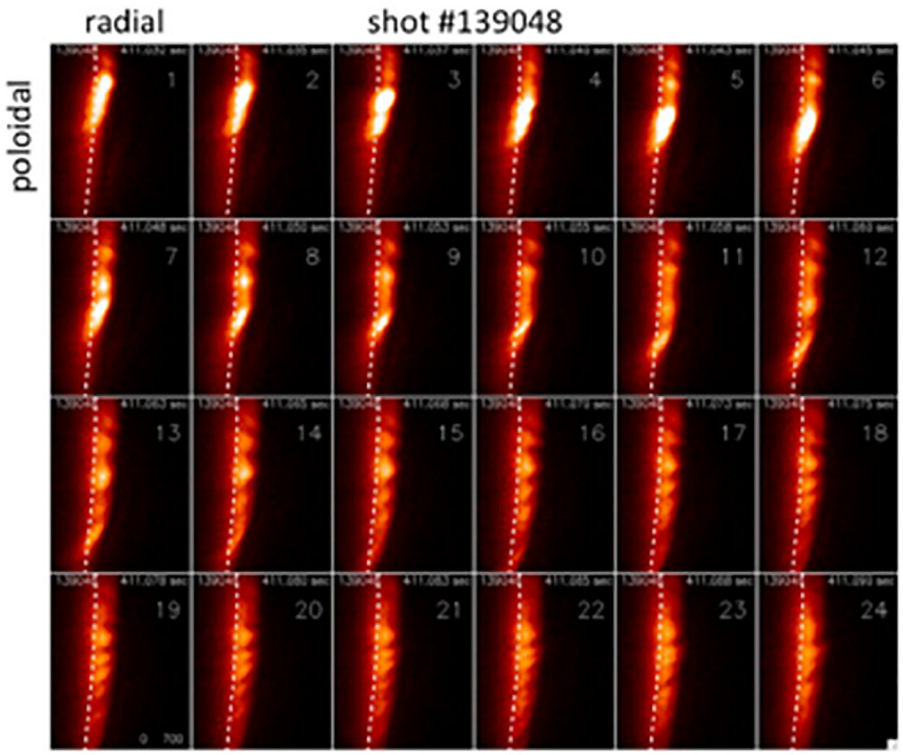

(b)

FIG. 2. Blob wakes in 24 frame sequences of raw GPI data for two shots (a) #139 053 and (b) #139 048. Each frame is a 24 cm (radial) $\times$ 30 cm (poloidal) region just above the outer midplane near the separatrix, and the frames are separated by 2.5 μs. The blobs enter from the top and the wakes form transiently as the blobs move downward. The separatrix (EFIT02) is shown by the thick dashed lines. The time during the shot (in ms) is shown at the upper right of each frame.

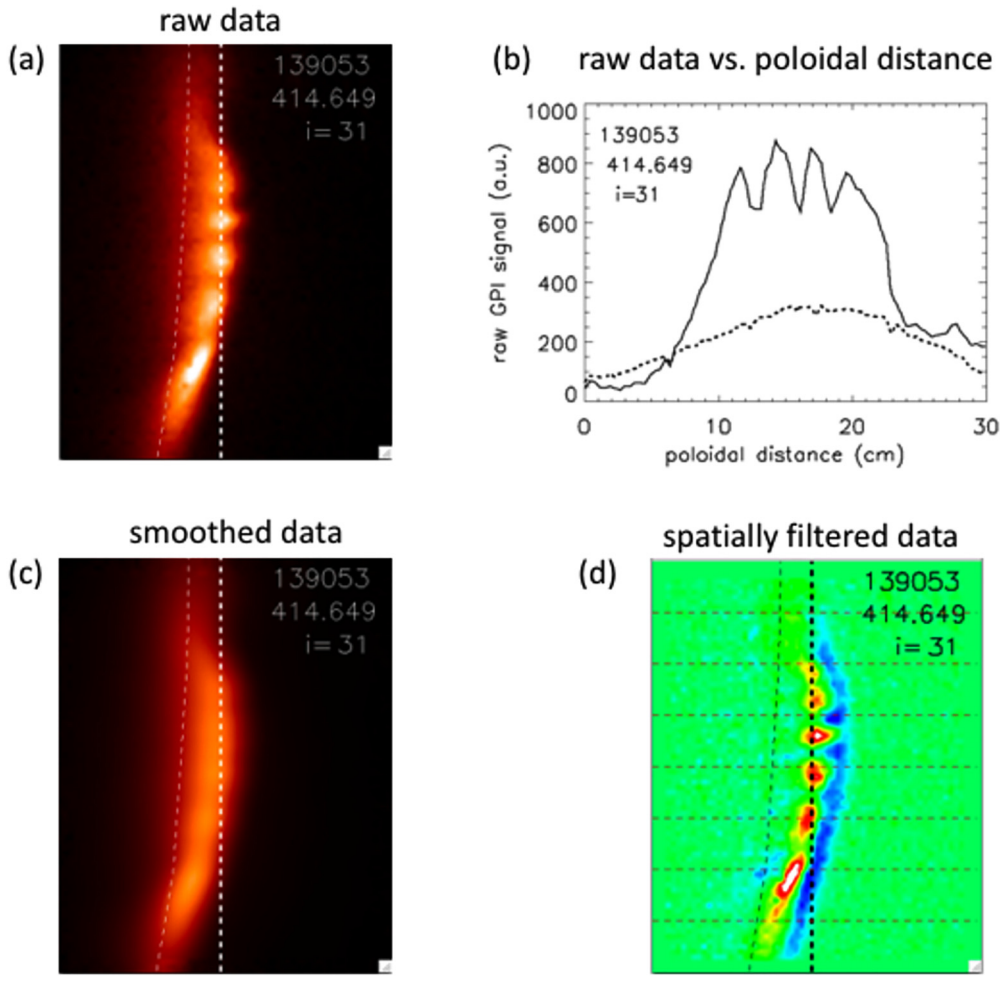

FIG. 3. Spatial high-pass filtering of the images. Part (a) is a single frame (#14) of raw data from Fig. 2(a), and (b) is the raw GPI data vs poloidal distance at the column i = 31 where the wake modulation is near maximum, along with the time-averaged data in this column over 1 ms (dashed line). Part (c) is the spatially smoothed frame, after boxcar averaging in both directions over 7 pixels (2.6 cm). Part (d) is the raw data frame minus the smoothed frame, now drawn using a color scale with red/white as maxima and blue/black as minima. The wake maxima are shown as red/white regions. The separatrix is shown as a thin dashed line, and horizontal grids are shown for reference with a vertical (i.e., poloidal) spacing of 5 cm.

C. GPI misalignment effect

One interesting feature seen in several shots of Fig. 4 (such as #139 048, #130 049, #139 058, and #139 059) is the systematic variation of the tilting of the blob wakes as a function of their vertical (i.e., poloidal) location within the GPI frame. This is illustrated in the frame in Fig. 5(a), taken from shot #139 048 in Fig. 4. Below the vertical center of the frame, the wakes appear to be tilted and extended toward the bottom-left to upper-right of the image, while above the center, the wakes appear slightly tilted in the opposite direction.

This tilting can be interpreted as due to the variable misalignment between the GPI viewing chords and the local magnetic field direction in the plane of the GPI emission, as discussed previously for NSTX data.[10] The spatial calibration data for the GPI target plane and camera view were incorporated into a GPI alignment code along with the magnetic equilibrium for each shot. The angles between the viewing chords (i.e., from the optical vertex to each camera pixel) and the local magnetic field direction at each pixel were calculated in the GPI target plane for maps such as shown in Fig. 5(b), where the contour lines show the magnitude of the angle between the GPI viewing chord and the local B field (in degrees), and the arrows indicate the relative magnitude and direction of the target plane component of the vector differences between the viewing chords and the magnetic field.

Figure 5(b) shows the magnetic field alignment map for the shot and time of Fig. 5(a), with the angular misalignments labeled on the contour lines, e.g., with a misalignment of $\Theta \sim 7.6^\circ$ labeled in dark blue (third level from the top). Perfect alignment is predicted only near pixel (i, j) = (43,49), i.e., just above the vertical center of the image and ~7 cm radially outside the wake location. The local misalignment directions for seven vertical locations along column i = 25 (the column near the maximum blob wakes for this shot) are shown as arrows, the lengths of which are proportional to the misalignment angle Θ. These two images in (a) and (b) are overlaid in Fig. 5(c). The tilting of the

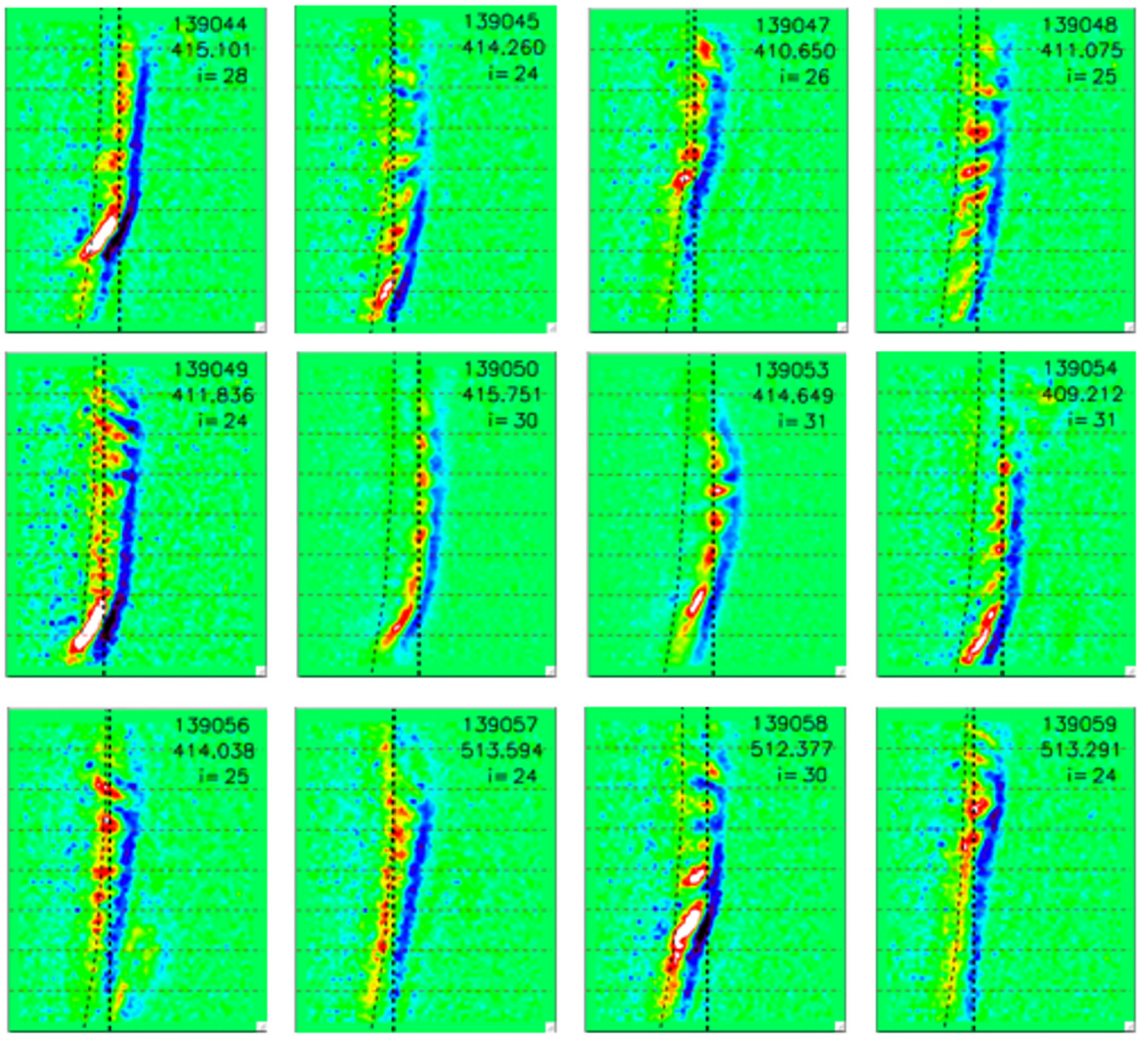

FIG. 4. Single frames from each of the 12 shots in Table I, showing the structure of the wakes after high-pass spatial filtering as in Fig. 3. The maxima of the wakes are shown as red/white regions. Vertical columns passing through the largest blob wakes are shown by black dashed lines (e.g., labeled, for example, as i = 28 in shot #139 044), and the separatrix is shown by the lighter vertical dashed line. Horizontal dashed lines are shown for reference with a vertical spacing of 5 cm.

blob wakes is well correlated with the direction of this misalignment, indicating that these apparent tilts are due to the viewing geometry and not to the wakes themselves.

The magnitude of the misalignments for the seven arrows in Fig. 5(b) varies in the range of $\Theta \sim 5^\circ$ to 13° (e.g., 5.7° at the vertical center), which will produce an apparent spatial "smearing" of field-aligned structures of $\delta \sim L_{II} \tan\Theta$, where $L_{II} \sim 12$ cm is the estimated GPI cloud length along the magnetic field lines.[10] For these angles, the range of smearing is thus $\delta \sim 1$–3 cm, which at the high end is close to the maximum visible extent of these wakes along the tilt direction in Fig. 5(a). Thus, the apparent structure of these wakes can be significantly affected by the angular misalignment, especially at the top and bottom of the image. Therefore, the wake identification and analysis below will use only the vertical pixels j = 20–60 out of 80, i.e., a poloidal extent of 7.5–22.5 cm within the 30 cm high image. At the vertical center (pixel j = 40), the tilt angle ranges from $\Theta = 4^\circ$ to 6° over all shots, while the average tilt over the chosen 15 cm vertical range is $\Theta \sim 7^\circ$, corresponding to a smearing distance of $\delta \sim 1.5$ cm.

Although the optical misalignment effect smears all structures in the image by the same amount (in cm), its effect on the small-scale wakes with a poloidal wavelength of ~3–4 cm can be significant, while its effect on the larger-scale structure of the blobs with a poloidal scale of ~12 cm (FWHM) is not significant. The cross-correlation (blob-sized) structures in the larger NSTX database were observed to be distorted by this effect only for misalignment angles $\Theta \geq 15^\circ$,[10] i.e., in poorly field-aligned shots. Further quantitative discussion of this misalignment effect on the results in the wake database is in Sec. III C.

D. Wake poloidal velocity

Figure 6(a) shows a single column of raw (unfiltered) GPI camera data but now plotted using the poloidal location in a single column

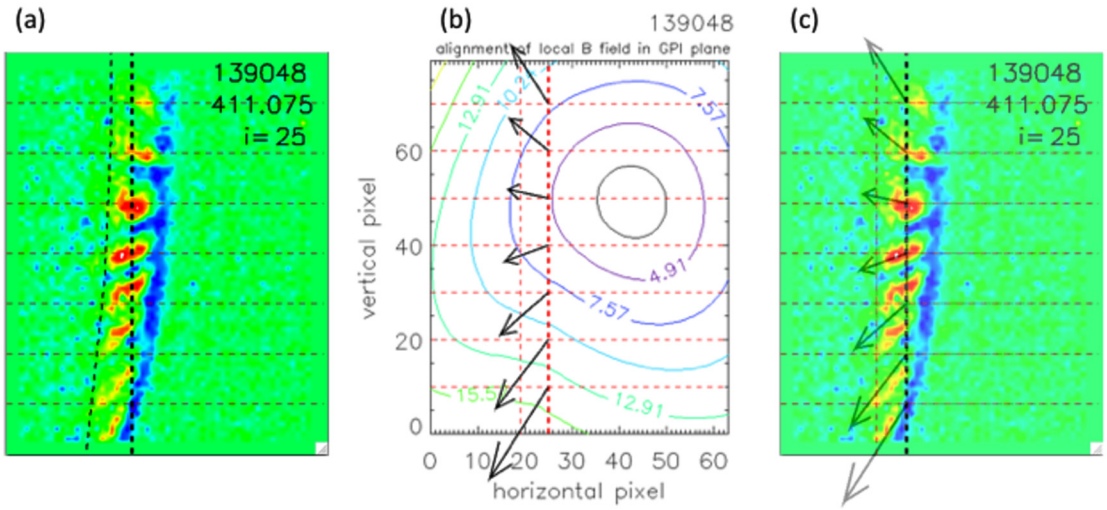

FIG. 5. Illustration of the misalignment effect in GPI images. The spatially high-pass filtered image in (a) is from shot #139048 of Fig. 4. Part (b) shows the contours of angular misalignment between the GPI view and the local magnetic field, with perfect alignment only at pixel (43, 49). The image in (c) is an overlay of (a) and (b), showing that the tilted wake structures tend to follow the local misalignment direction.

(vertical) vs time (horizontal). This particular plot is for shot #139 053 and column #31 (where the wake is maximum), as previously shown in Fig. 2(a). This display allows the poloidal velocity of the blobs and wakes within this column to be seen directly from the slope of the signal maxima.

The top of Fig. 6(a) shows the blob poloidal motion over a relatively long time scale of ∼4.4 ms (1750 frames), with the blobs apparently distributed randomly in vertical position and time, but with a systematic trend for downward motion vs time in the ion diamagnetic drift direction. Note that the blobs are also moving radially outward to some extent and so do not remain in a single column for their whole lifetime. At the bottom of Fig. 6(a) are the same data plotted over a faster time scale of 0.63 ms (250 frames), starting from the first frame at the left of the top image. The blob motion toward the lower right can be seen more clearly, and now, the wake motion can also be seen as ribbons or waves of modulation moving upward to the right, i.e., in the electron diamagnetic drift direction. The bright ribbons within the first 100 μs of this plot correspond to the modulations shown in Fig. 2(a) for this shot (#139 053) in this column (i = 31), which have a duration of ∼25–50 μs. Another wake with about 10 modulations can be seen in the third 100 μs of this plot, which show the poloidal velocities varying with space and time. Note that not all of the wakes are present in a single frame (i.e., a single time in this plot), and not every blob has a wake in this chosen column.

Figure 6(b) shows the same type of plots for shot #139 048 and column #25, which is the case previously shown in Fig. 2(b). The blob motion is again downward and the wake motion is upward. For example, there are about 15 nearly periodic wakes visible in the 4th 100 μs time period in the bottom part of this figure. The approximate blob and wake velocities as shown by the yellow arrows are ∼3 km/s downward (i.e., in the ion diamagnetic direction) for the blob and ∼4 km/s upward for the wake. The downward poloidal blob velocity corresponds to the E × B drift direction, whereas the wakes are propagating in the opposite direction (see also Sec. III D).

E. Wake identification

Ideally, the identification and characterization of blob wakes in the GPI camera data should be done using a computational algorithm motivated by previous empirical data or a specific hypothesis or theory. However, since this paper presents the first description of blob wakes and since there is a significant variation of wake characteristics in the data, it is difficult at present to define such an algorithm. Therefore, we will describe a process by which the initial identification of the clear blob wakes is done "by eye" followed by an automated analysis to estimate the main characteristics of these wakes.

The initial classification of wakes by eye is done using plots such as those shown in Fig. 7. These plots show the GPI camera data for the chosen columns [e.g., i = 25 Fig. 6(a)], as a function of time (as in Fig. 6), but now with spatial filtering as done in Figs. 2 and 3 (i.e., subtraction of the spatially smoothed images), and also with an additional normalization (i.e., division) by the spatially smoothed frame to further highlight the smaller-scale wake structures.

Figures 7(a)–7(d) show these normalized data for 1 ms periods for 4 selected shots. These plots have been rebinned with linear interpolation for visual clarity to have 3× the original number of pixels in the vertical direction (i.e., 3 × 80 = 240) and 6× the number of original pixels in the time direction (i.e., 6 × 397 = 2382). The color is scaled from −0.5 (black) to 0.5 (white) in these normalized amplitude units. Note that the starting time of each plot is offset from the time of the peak GPI signal (412 ms) by an integral number of millisecond (e.g., −1 ms for #139 048), as indicated by "toff" at the top left of each plot.

The space vs time data in each of these plots are then divided into 19 time segments of 50 μs each (which is the approximate duration of the wakes), as shown by the white dashed lines and numbered 0–18 below each segment. These segments are also constrained to the poloidal range 7.5–22.5 cm (i.e., pixels j = 20–60 out of 80), as shown by the horizontal white dashed lines, in order to minimize the GPI alignment variations of Sec. II C. Each rebinned segment is therefore 120 × 120 pixels in the format of Fig. 7. These segments were then

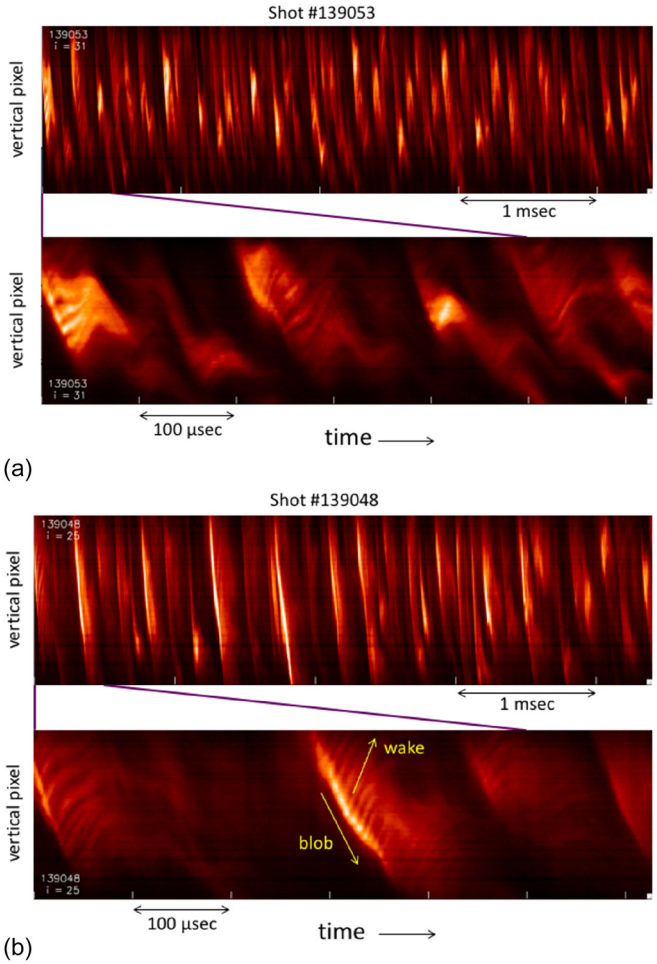

FIG. 6. Poloidal blob and wake velocities illustrated using a single column of raw GPI data plotted vs time. This column is chosen to be near the maximum of the blob wake modulations in Fig. 4. The top parts of (a) for shot #139 053 and (b) for shot #139 048 are on a slow time scale (4.4 ms) and the bottom parts over a shorter time scale (0.63 ms). The blobs move downward vs time, while the wakes move upward vs time in this plot. Note that the blobs can move radially out of this column, and not all wakes are present in any single frame.

scanned by eye to identify wake structures for further analysis, such as those visible in segments #1 and #7 in Fig. 7(a). The clarity of the observed wakes is rated as follows: W3 (very clear), W2 (clear), W1 (marginally visible), and W0 (not visible), as shown by the labels below each segment in Fig. 6. Obviously, this process is only for guidance as to which segments to use in the subsequent automated analysis and is not an quantitative measure of the wake strength.

In the four selected cases of Fig. 7, there are a total of 12 segments identified with clear wakes (W2 or W3), out of a total of $19 \times 4 = 76$ segments. This is higher than the average fraction of segments with clear wakes, since these particular shots/offset times were selected to illustrate the wake identification process (see also Sec. II G). The angle of these wakes in these plots corresponds to the wake velocity in the poloidal direction; for example, an angle of $\theta = 45°$ clockwise with respect to the vertical direction corresponds to a poloidal wake velocity of $V_{pol} = 15\,\text{cm}/50\,\mu\text{s} = 3\,\text{km/s}$ in the upward (electron diamagnetic drift) direction. Most of the clear wakes have angles $\theta \leq 85°$, with only a few exceptions such as segment #13 of Fig. 7(c) and segment #6 of Fig. 7(d). Most of the clear wakes have a poloidal wavelength of $\lambda_{pol} \sim 3$–4 cm in the vertical direction in these plots. More quantitative analysis is discussed below.

We note at this point that a previous analysis of blobs for 9/12 shots in the present database[4] showed an average poloidal size scale of the blobs to be $L_{pol} = 12.6\,\text{cm}$ (FWHM) within the radial range 0–4 cm outside the separatrix, which is much larger than the wake wavelength. That analysis also showed an average blob poloidal velocity of 1.2 km/s in the ion diamagnetic (downward) direction, which is opposite to the wake direction for almost all cases in Fig. 7. Further comparisons of blobs and wakes will be discussed in Sec. III B.

F. Wake analysis

The main characteristics of the clear wakes identified as W2 and W3 in the space vs time plots like Fig. 7 were analyzed one segment at a time using an algorithm designed to quantify the subjective wake identification process. The idea is to rotate each 120×120 pixel segment of space vs time around its center to find the direction in which the standard deviation of the signal variation is maximized, which is assumed to be perpendicular to the wake propagation direction. The wake velocity is then determined from this rotation angle. The wake amplitude is determined from the fluctuation level (i.e., standard deviation) of the normalized signal perpendicular to the wake velocity (in this mixture of space and time coordinates), and the poloidal wavelength of the wake is inferred from a spatial Fourier analysis of these fluctuations and a projection into the poloidal direction.

The implementation and limitations of this process are discussed in detail for one example in the Appendix. Obviously, this analysis averages over the wake structures in each space-time segment and so gives only a first approximation to the instantaneous wake characteristics.

Six examples of the inferred wake directions and wavelengths are compared with the original space vs time segment data in Fig. 8, where each case corresponds to one of the clear wake segments shown in Fig. 7. For example, the comparison in Fig. 8(a) corresponds to segment #7 in Fig. 7(a), where the normalized raw data are at the left and the calculated wake direction and wavelength are shown as a sine wave at the right (the relative wake amplitudes were not used). The rotation angles such as $\theta = 40°$ in Fig. 8(a) are measured with respect to the vertical (poloidal) direction, and the wavelengths such as $\lambda_{pol} = 3.9$ cm are calculated in the poloidal (vertical) direction. For this case, the rotation angle of 40° corresponds to a poloidal wake velocity of $V_{pol} = 3.6\,\text{km/s}$ in the upward (electron diamagnetic drift) direction in the lab frame of NSTX. The ranges of poloidal velocities and wavelengths shown in these cases are $V_{pol} = 1.1$–$3.6\,\text{km/s}$ in the electron direction and $\lambda_{pol} = 2.9$–4.1 cm. The wake amplitudes for the segments of Fig. 8 were in the range of $A = 0.015$–0.031, which are higher than the average segment amplitude over the whole database (0.009), since these cases were chosen to show clear wakes. Note that these wake amplitudes are relative values only and not equivalent to the fluctuation levels of the wakes in the raw data, due to the spatial filtering and normalization. The distribution of wake amplitudes is discussed further in Sec. II G.

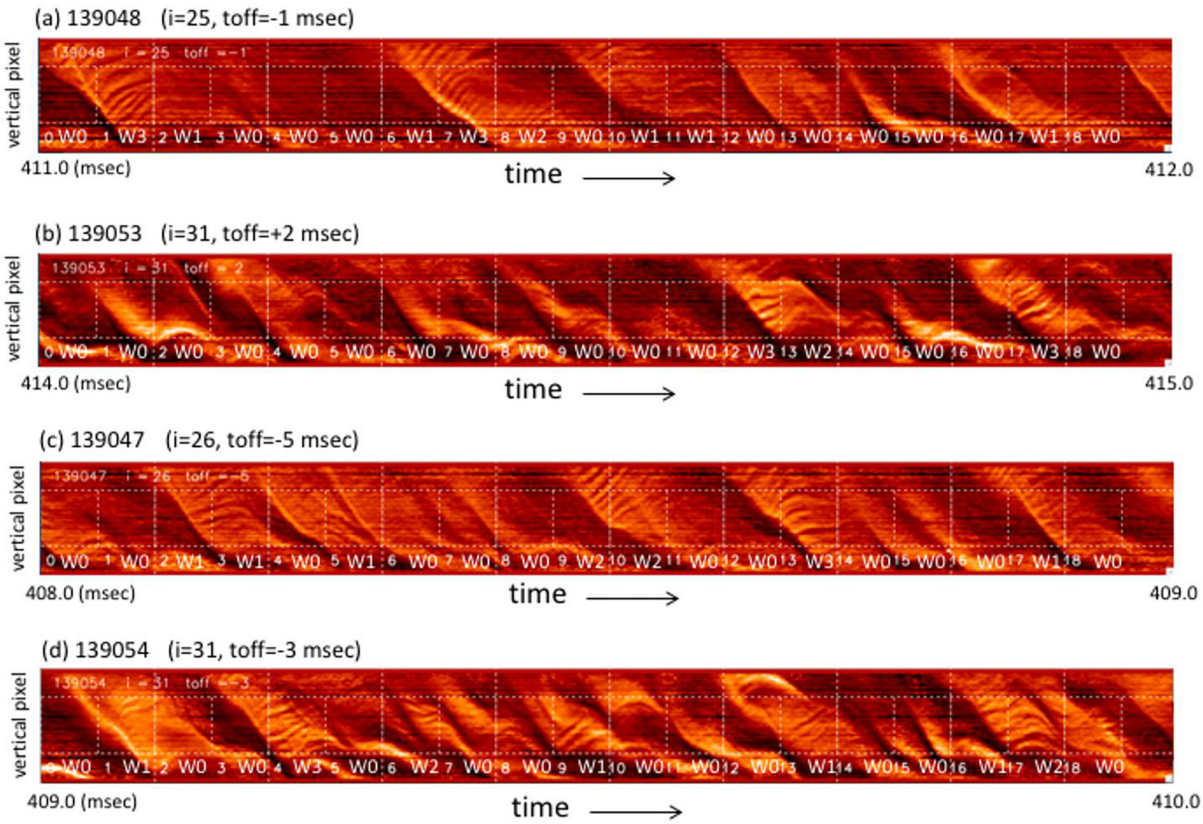

FIG. 7. Examples of blob wake identification for 1 ms time intervals for four selected shots. In each case, the raw GPI data are plotted with the poloidal coordinate as vertical and time as horizontal (as in Fig. 6), using the column number and time offset written at the upper left of the plot. For these plots, the spatially smoothed data are divided by the smoothed frames to further emphasize the small-scale structure of the wakes (see Sec. II E). The data for each shot are divided into 19 time segments of 50 μs duration (20 frames), as shown by dashed white lines and numbered at the bottom left of each segment. The data are also segmented using only the middle 40 rows of the GPI column, also indicated by dashed white lines. The clarity of the wakes in each segment is indicated by the labels W0–W3, where W2 and W3 are the clearest wakes.

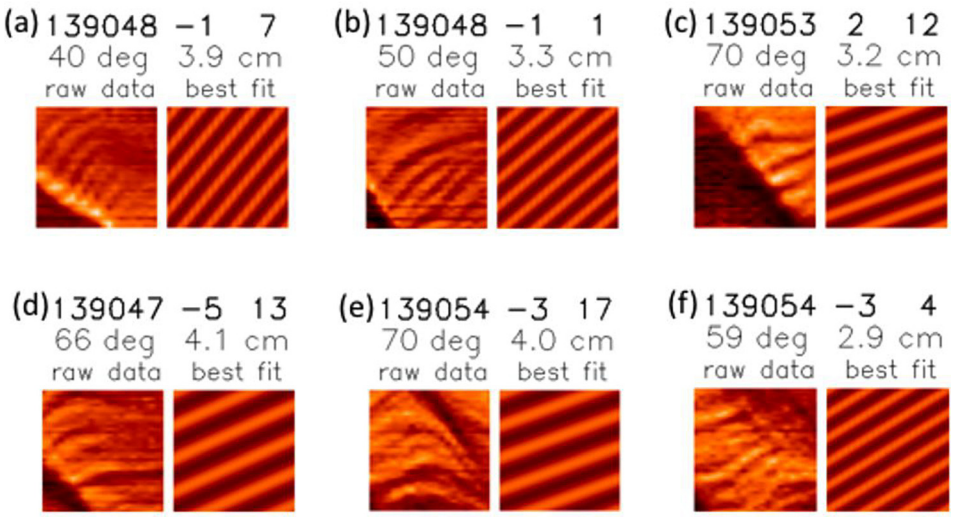

FIG. 8. Examples of wake analysis for six selected data segments. Each part (a)–(f) shows one segment of raw data at the left and the best fit to the wake angle and wavelength derived from the analysis as described in Sec. II F and the Appendix. The cases are labeled at the top by the shot #, offset time from the peak GPI time (in ms), and segment number, e.g., 139 048, −1, 7 for case (a). The optimum rotation angle and poloidal wavelength are also written for each case.

These cases illustrate some of the limitations of this wake analysis method. The wake structures often curve significantly within a segment, as seen in Figs. 8(d) and 8(e), so that the inferred wake velocities represent only an average over the varying wake velocity variations. The present alorithm also finds only one average wavelength in each segment and so does not try to infer the distribution of wake wavelengths such as seen in Figs. 8(d) and 8(f). The calculated amplitude of the wake structures depends on the extent to which the wakes fill the segment, and so wake structures which are not well centered such as those shown in Figs. 8(c) and 8(f) have a lower than expected amplitude. The present wake amplitude analysis is also imperfect due to the contributions from the edge of the blob structures, which are not completely suppressed by the spatial filtering. Less obvious is a limitation in the automated rotation angle search to within 0°–85° from the vertical, which limits the inferred rotation speeds to $V_{pol} \geq 0.3$ km/s in the upward (electron diamagnetic drift) direction, for reasons described in the Appendix. Thus, the present wake analysis is intended to give only an initial survey of typical wake characteristics, as summarized in the wake database below.

G. Wake database

The blob wake analysis described above (and in the Appendix) was applied all to the 12 shots in Table I for each of 11 separate 1 ms time periods starting from −5 ms before to +5 ms after the peak of the GPI signal, which is the usual time period for blob analysis in the NSTX GPI data.[4] Thus, the number of 50 μs time segments contained in this database was 12 shots × 11 time periods × 19 segments/time period = 2508 segments. For each of these segments, the clarity of the wakes was evaluated by eye as described in Sec. II E on a scale from W3 (very clear), W2 (clear), W1 (marginally visible) to W0 (not visible). The result was 92 or 4% of segments with very clear or clear wakes (W3 + W2), 455 segments or 18% with visible wakes (W1 + W2 + W3), and the remaining 78% of the segments with no visible wakes. Thus, the clear blob wakes evaluated this way were fairly rare.

The main results from this wake analysis database are shown in Fig. 9. Figure 9(a) shows the calculated wake amplitude vs the wake clarity as evaluated by eye for the entire database. The wake amplitude increases systematically with the wake clarity as estimated by eye, as expected, but there is also a significant scatter in the results as shown by the standard deviations, which suggests that either the evaluation by eye or the amplitude algorithm is inaccurate (or both). This is not too surprising, given the limitations and approximations discussed in Sec. II F and in the Appendix, for example, the assumption of the algorithm that the wake fills the segment. The amplitudes of the wake segments used for illustration in Fig. 2 and in the Appendix were 0.027 (about average for W3) and 0.015, respectively.

The poloidal velocity for the 92 clear wake segments in this database (i.e., W2 + W3) is shown in Fig. 9(b) as a function of the wake amplitude. The average wake velocity is $V_{pol} = 1.5 \pm 1.0$ km/s in the upward (electron diamagnetic) direction. This includes 15/92 segments at the lowest accessible poloidal velocity of $V_{pol} = 0.3$ km/s, which was limited by the maximum rotation angle of 85° in this algorithm (see the Appendix). There appears to be a slight trend for decreasing wake velocity at higher wake amplitude, as shown by the dashed line (linear fit to the data) in Fig. 9(b). The most important aspect of this result is that the poloidal direction of these wakes is opposite to that of blobs in the same set of data, which moved at $V_{pol} = -1.2 \pm 1.2$ km/s in the ion diamagnetic direction within the region 0–4 cm outside the separatrix for these shots (see the discussion in Sec. III B).

The poloidal wake wavelength λ_{pol} for these 92 clear wake segments is shown in Fig. 9(c) as a function of the wake amplitude. The average poloidal wavelength from this analysis is $\lambda_{pol} = 3.5 \pm 0.7$ cm. However, note that the spatial smoothing in the wake analysis filters out with wavelengths roughly $\lambda_{pol} > 6$ cm, while the GPI optical resolution filters out wakes with roughly $\lambda_{pol} < 2$ cm. Within this range, there seems to be no significant variation of this wavelength with respect to the wake amplitude in this database, as shown by the dashed line (linear fit). The most important aspect of this result is that the wavelengths of the wakes are significantly smaller than the scale of the blobs in this database, which have an average poloidal scale of $L_{pol} = 12.6$ cm FWHM (see Sec. III B).

The dependence of wake V_{pol} vs λ_{pol} for the 92 clear wakes in this database is shown in Fig. 9(d). The clustering of points in the curved lines labeled H = 3–6 is due to the choice of a single average poloidal Fourier harmonic number H for each wake, which is used along with the wake angle to estimate both the wake velocity and wavelength, as discussed in the Appendix. There seems to be a systematic increase in V_{pol} with λ_{pol}, as shown by the dashed line (linear fit).

H. Shot-to-shot variations

The 12 shots in this database (listed in Table I) were all taken from one NSTX experiment[12] and had relatively minor differences in their global plasma conditions. For example, the applied NBI heating power was 6 MW to well within 10%, the B/I ratio was constant to within ±10%, the outer midplane separatrix position was $R_{sep} = 147.3 \pm 0.4$ cm, and the plasma shapes were nearly constant. However, the local B field misalignment at the GPI puff (see Sec. II C) was not quite constant: For example, at the vertical center of the chosen column for each shot, the misalignment angle varied from $\Theta = 4.0°$–$6.4°$. Previous analysis of blob smearing effects showed misalignments of $\Theta \leq 15°$ to have a relatively little effect on blob correlation functions,[10] but the smearing of small-scale wakes will be more significant at low misalignment angles, as discussed in Sec. III C.

The details of the shot-to-shot variations within the database are shown in Table II. The number of 50 μs time segments with visible wakes (W1 + W2 + W2) varied from a high of 71 for shot #139 053 (i.e., 34% of the 19 × 11 = 209 segments) to a low of 19 for three shots (i.e., 9% of segements). There was also a surprisingly large variation in the number of clear and very clear wakes (W2 + W3) vs shot, from a high of 27/209 segments (13%) for #139 053 and 17/209 segments for #139 048 (which were the shots used for illustration in Figs. 2, 3, and 6) to a low of 0/209 segments for shots #139 056, #139 057, and #139 059. However, the average wake amplitude vs shot (averaged over all segments) varied from $A = 0.013 \pm 0.005$ (#130 953) to $A = 0.006 \pm 0.002$ (#139 057), which is only a marginally significant difference. There was a relatively little shot-to-shot variation in the number of big blobs over the same 10 ms interval (see Sec. III B) or in the wake wavelength or poloidal velocity as evaluated for the set of W2 + W3 wakes, as shown in Table II. Further discussion of these variations is in Sec. III C.

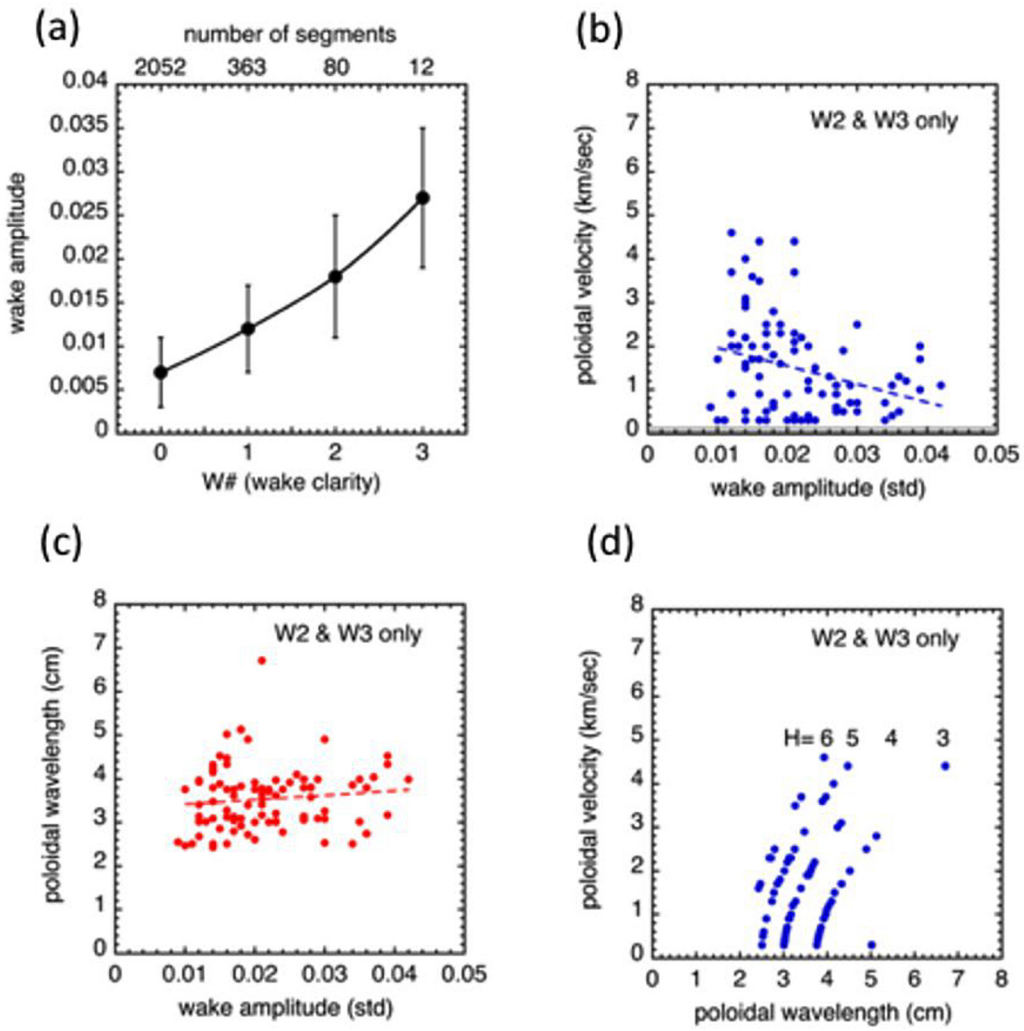

FIG. 9. Results from the blob wake database containing a total of 2508 segments of 50 μs duration. (a) is the wake amplitude vs the wake clarity evaluated by eye, where the former is the result from the wake analysis (see the Appendix) and the latter uses the qualitative wake scale W3 (very clear) to W0 (not visible). The number of segments in each wake category is written at the top. (b) is the estimated poloidal velocity V_{pol} vs the wake amplitude obtained from the wake analysis of the clear wakes only (W2 + W3). The average value is $V_{pol} = 1.5 \pm 1.0$ km/s, including the points at the edge of the accessible region (the shaded region is not accessible). (c) is the poloidal wavelength of the wake vs the wake amplitude of the clearest segments only, with an average value of $\lambda_{pol} = 3.5 \pm 0.7$ cm. (d) is V_{pol} vs λ_{pol}, which both depend on the inferred poloidal harmonic number H. The dashed lines are linear fits.

III. DISCUSSION

This section first summarizes in Sec. III A the experimental results on blob wakes and then in Sec. III B discusses the connection between blobs and wakes in the present database. Section III C describes possible causes for the observed shot-to-shot variation in blob wakes, and Sec. III D discusses theoretical interpretations of blob wakes. Section III E describes possible future directions for this research.

A. Summary of results

This paper described the first observations and an initial analysis of blob wakes, which are transient small-scale fluctuations formed just after the passage of poloidally moving blobs in the SOL of NSTX. Clear wakes were initially identified by eye from raw GPI camera data using plots like those in Fig. 7, and then a database was constructed from a set of 12 high power H-mode plasmas. About 100 examples of clear blob wakes were seen in that database, with an average poloidal wavelength of $\lambda_{pol} \sim 3.5$ cm (i.e., considerably smaller than blobs) and an average poloidal velocity in the electron diamagnetic direction of $V_{pol} \sim 1.5$ km/s (i.e., the opposite direction to that for blobs), as summarized in Fig. 9. This initial analysis was limited to a wavelength range $\lambda_{pol} \sim 2$–6 cm and poloidal velocity range $V_{pol} > 0.3$ km/s. There was a significant shot-to-shot variation in the frequency of clear blob wakes within this database, ranging from a high of 13% of the data segments to a low of 0% (see Table II).

TABLE II. Wake statistics vs shot (10 ms interval).

Shot	W1 + W2 + W3 (all wakes)	W2 + W3 (clear wakes)	Big blobs (norm ≥ 2)	A[a] (ave.)	λ_{pol}[b] (cm)	V_{pol}[b] (km/s)	Θ[c] (deg)	Φ[c] (deg)	|δz| (cm)	Δr (cm)
139 044	33	7	45	0.010	3.5	1.9	5.5	206	0.51	2.2
139 045	21	1	30	0.006	2.4	1.6	5.8	188	0.17	0.75
139 047	51	15	50	0.008	3.4	1.7	6.0	204	0.51	1.1
139 048	51	17	38	0.009	3.7	2.7	5.7	200	0.41	2.2
139 049	19	1	28	0.007	4.5	2.0	6.0	189	0.20	1.1
139 050	62	7	54	0.009	3.3	1.4	4.6	192	0.20	2.6
139 053	71	27	51	0.013	3.6	2.1	4.1	187	0.10	3.7
139 054	51	9	48	0.013	3.4	1.5	4.4	196	0.25	3.4
139 056	31	0	64	0.006	…	…	6.3	157	0.52	0.75
139 057	19	0	35	0.006	…	…	6.3	166	0.32	0.0
139 058	27	8	31	0.013	2.9	1.5	5.0	212	0.56	2.6
139 059	19	0	32	0.006	…	…	6.3	206	0.58	0.37

[a]Amplitude averaged over all segments.
[b]Averaged over clear wakes W2 and W3.
[c]Evaluated at the vertical center j = 40.

B. Wakes vs blobs

From the 2D frames of raw GPI data as illustrated in Fig. 2, it appears that the clear wakes form just after the passage of blobs in both space and time. In these cases, the blob motion was mainly poloidal (vertical), as usual in high-power H-mode shots in NSTX.[4] The blob structures were less clear in the space vs time plots of Fig. 7, which were spatially filtered to highlight the smaller-scale structure of the wakes.

A striking feature of the wakes which was not analyzed in Sec. II is that the wakes appear to peel off one-at-a-time at the top edge of the blob as it moves downward, as illustrated in Figs. 2, 6, and 7. The wakes then move upward while the blob moves downward, leaving behind a trail of wakes with a roughly constant spatial wavelength, as illustrated in Fig. 4. The frequency of the wake generation can be seen, for example, at the bottom of Fig. 6(b), where 8 wakes are created in ∼43 μs near the center of the panel, giving a wake frequency of up to $f_{wake} \sim 200$ kHz (or wake period of ∼5 μs). This wake generation frequency may also be related to the spatial pattern of wakes using $f_{wake} \sim V_{pol}/\lambda_{pol}$, which gives an average $f_{wake} \sim 40$ kHz for the entire database of 92 clear wakes of Fig. 9. If so, then the increase of the wake wavelength with wake velocity shown in Fig. 9(d) may be explained by a roughly constant wake generation rate, such that the wake wavelength increases with the wake velocity.

The number of blobs per shot in the SOL in the same 10 ms time interval with a normalized amplitude of ≥2 and an area of ≥14 cm^2 (100 $pixels^2$) is also shown in Table II. There was an average of 42 ± 11 of such big blobs per shot, compared with an average of 7.6 ± 8.4 clear wakes per shot (W2 + W3) and 38 ± 18 visible wakes per shot (W1 + W2 + W3). Thus, the average number of clear wakes per big blob was ∼18%. However, the cross-correlation coefficient between the number of these big blobs and the number of clear wakes across these 12 shots was only 0.31 (comparable to the random correlation level), and the cross-correlation coefficient between clear wakes and smaller blobs with a normalized threshold amplitude of ≥1.5 was only −0.2, although the cross-correlation between the number of big blobs with the number of all visible wakes was somewhat larger (0.63).

The relationship between the blob amplitude and wake formation is illustrated in a different way in Fig. 10, which plots the GPI signal levels at two single pixels vs time, along with the times of clear wake segments. These two pixels were chosen at +7.5 cm and 0 cm above the vertical center of the image (i.e., at j = 60 and 40) in the columns used for evaluating the wakes, and their signal levels were normalized by their time-average over these 1 ms periods. Large blob events in this plot correspond to a normalized signal level of roughly ≥2, which occurs ≤10% of the time during these 1 ms intervals. The clear wake segments W2 and W3 are indicated by red boxes of 50 μs duration (the wakes themselves are difficult to see in these signals).

It appears that the clear wake segments in these cases do not always correspond to the largest blob events seen in these pixels and that some clear wake events correspond to relatively small blobs with a normalized amplitude ≤2; thus, the largest blobs do not always correlate with the clearest wakes. However, the blobs are not perfectly identified by the amplitudes at these chosen pixels, and other blob characteristics may better correlate with the observed wakes. Note that the relative timing between the wake segments and the blob signals is uncertain by at least ±50 μs due to the wake time segmentation and to the blob propagation time poloidally over the distance between these pixels. The average time delay of ∼25 μs between the signals in the two pixels in Fig. 10 (determined from cross-correlation analysis) gives an average poloidal velocity of ∼3 km/s downward for the fluctuations in these cases, which is roughly the blob velocity.

The relationship of blobs and wakes was further tested using the large database described in Sec. II G. The blob level was evaluated as the average of the raw signal level over the whole of each space/time segment used to evaluate the wakes (i.e., the dashed boxes in Fig. 7). This set of average signal levels did not correlate significantly with the wake clarity levels W0–W3, consistent with Fig. 10. Thus, there is so far no evidence that wake clarity depended on the blob amplitude in this database. Other properties of blobs might trigger the wake

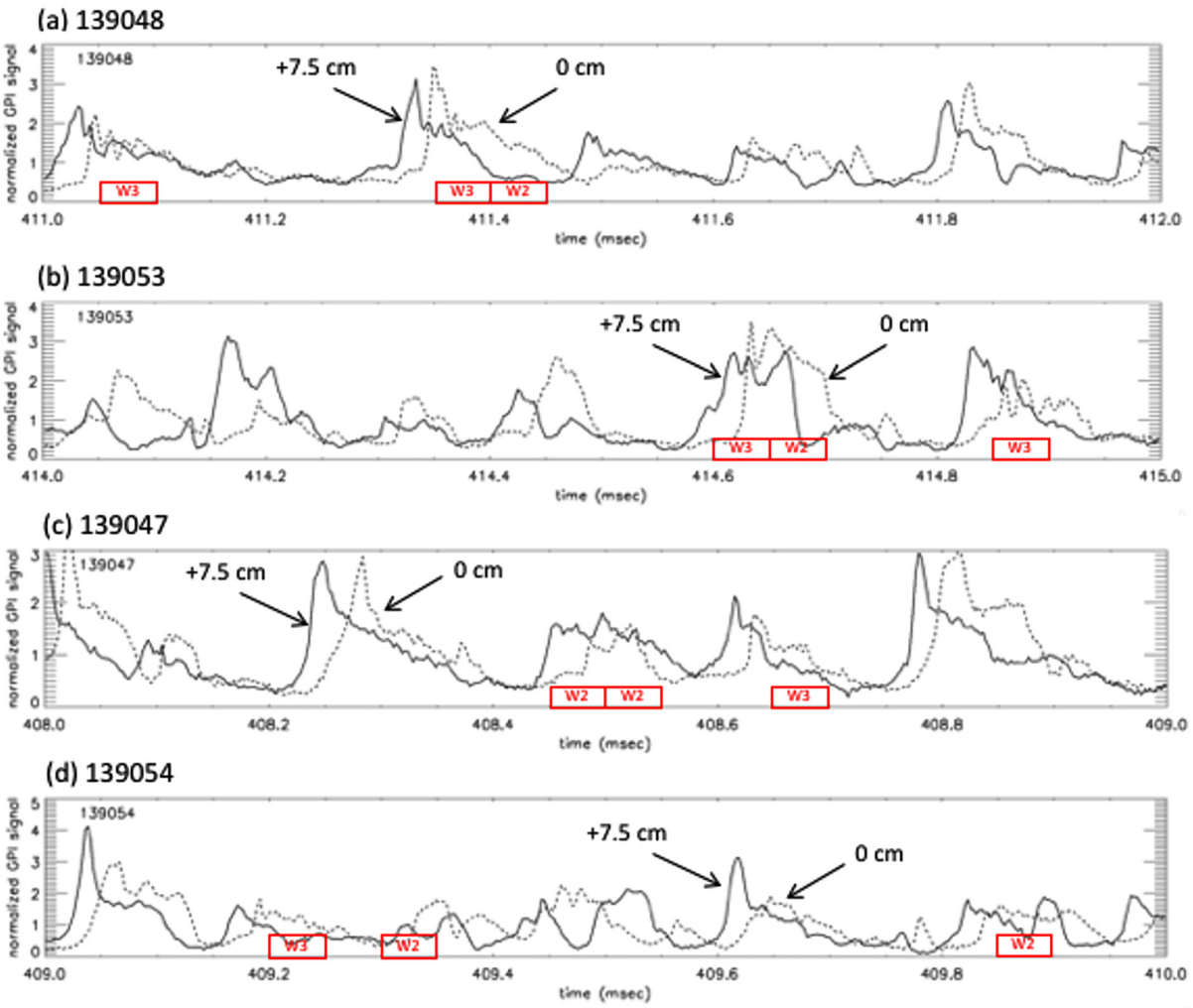

FIG. 10. Comparison of the normalized GPI signals and wake timing for the same shots/times as in Fig. 7. The GPI signals are shown for two pixels at 7.5 cm (solid) and 0 cm (dashed) with respect to the vertical center of the images at the wake analysis columns. The clear wake segments are indicated by the red boxes below. The clear wakes do not always correlate in time with the largest blobs. The relative timing of the blobs and wakes is uncertain by at least $\pm 50\ \mu$s due to the segmentation of the wakes and to the propagation time of blobs across these segments.

formation, but these are not apparent in the movie data due to the complexity and variability of the blob structure and motion.[14] Thus, the exact cause of the wake formation is not yet understood, which is not too surprising since the cause of blob formation is not well understood either.

C. Causes of wake variation

It was noted in Sec. II H that there is a significant variation in the number of wakes per shot and their size and speed within the present database, as shown in Table II and illustrated in Figs. 7–9. The shot-to-shot variation in the number of wakes is surprising given the similarity of these shots as discussed in Sec. I C; for example, from a high of 13% of segments having clear wakes (#139 053) to a low of 0% having clear wakes (#139 056, 139 057, and 139 059). To help understand the wakes, it would be useful to understand these variations.

As mentioned in Sec. II B, the number of large blobs with a normalized signal level ≥ 2 was not well correlated with the shot-to-shot variation in the number of clear wakes, and this lack of correlation also holds for the number of blobs with a normalized signal level of ≥ 1.5. Thus, the blob generation rate is not the dominant cause of the variation in the number of clear wakes per shot over this database.

Another possible cause of the shot-to-shot variation is the variable misalignment of the GPI viewing angle Θ with respect to the local B field angle, as discussed in Sec. II C. This misalignment causes an apparent spatial smearing of any field-aligned structure by $\delta \sim L_{II} \tan\Theta$ along the direction of misalignment, where $L_{II} \sim 12$ cm is the estimated GPI cloud length along the magnetic field lines.[10] It is interesting that in Table II, the shot with the largest number of clear wakes

had the smallest misalignment angle of $\Theta = 4.1^\circ$ (evaluated at the vertical middle $j = 40$), and the three shots with no clear wakes had the largest misalignment angles of $\Theta = 6.3^\circ$–6.4°. Averaged over all shots, the cross-correlation coefficient between the number of clear wakes and the misalignment angle is relatively high (−0.7).

The estimated spatial smearing of wakes in Table II varies from $\delta = 1.3$ cm for the largest misalignment to $\delta = 0.8$ cm for the smallest misalignment (evaluated at the vertical image center). The estimated smearing in the poloidal (i.e., z) direction is roughly $\delta z \sim L_{II} \tan\Theta \sin\Phi$, where Φ is the direction of the misalignment vector measured with respect to the outward radially direction. For the estimated range of $\Phi = 157^\circ$–210° in Table II (again at the vertical image center), the magnitude of the estimated poloidal smearing δz varies over the range $\delta z = 0.1$–0.6 cm, which at the high end is enough to significantly reduce the poloidal modulation amplitude of wakes with $\lambda_{pol} \leq 2$ cm. Thus, the variable smearing due to these relatively small misalignments could cause at least some of the shot-to-shot variations in these small-scale wakes. A more accurate analysis is needed to confirm this, including, for example, the GPI optical resolution limit of ∼0.5 cm and a more accurate GPI cloud length.

Another variable in Table II which correlates with the shot-to-shot variation in the number of clear wakes is the radius chosen for the wake analysis, which was based on the location of the clearest wakes as seen by eye in the movie data. These radii are shown as vertical lines in Fig. 4, and their distances Δr outside the local separatrix (at the vertical center) are in the range of $\Delta r = 0.0$–3.7 cm (see Table II). These radii were located near the most common blob radius, which varies from shot-to-shot, even though the calculated separatrix locations were all within 1.5 cm of each other (Table I). There is a high correlation in Table II between the number of clear wakes and the wake analysis radius Δr (correlation coefficient ∼0.7) and a very high correlation (0.94) between wake analysis radius Δr and misalignment angle Θ, since the misalignment is systematically lower at larger radii by ∼2°–3°/4 cm (near the vertical center), as illustrated in Fig. 5(b). Thus, some of the shot-to-shot variation in the number of clear wakes can also be attributed to the small variations in the radial locations chosen for this wake analysis.

The cause of these small shot-to-shot variations in the wake locations is not yet understood. An examination of the Thomson scattering profiles at the times of interest showed no significant correlation between the local density or electron temperature measured at points within about ±1 cm of the separatrix and the number of clear wakes in that shot (see Fig. 2 of Ref. 10 for a typical edge density profile). However, since the Thomson scattering data do not provide accurate SOL density or temperature profiles, it remains possible that wakes are more likely for some specific SOL profiles.

In shots with many clear wakes, there is also a significant variation in the number of wakes per unit time within a single shot (as in Figs. 7 and 10) which cannot be explained by the B field misalignment or average blob location, which are nearly constant over the 10 ms of analysis. However, even if the average plasma conditions are constant during a shot, the individual blobs differ substantially from each other; for example, there is a significant spread in the blob amplitude, size, ellipticity, tilt angle, velocity, trajectory, and time between blobs within a given type of H-mode shot in NSTX,[4] and similar blob variations have been seen on other devices.[5–9] From the videos of the raw data,[14] it appears that each clear wake occurs just after a blob in space and time but that not all blobs have wakes after them. Apparently, some aspect of the individual blob triggers the wake formation, for reasons not yet known.

D. Theoretical interpretations

The observation of wakes presents an interesting opportunity and challenge to theory and modeling. In this section, we discuss the strengths and weaknesses of some possible explanations.

As far as we are aware, no numerical simulations have seen blob-triggered wakes that bear a qualitative resemblance to the wakes shown in this paper. This may not be surprising, since blob wakes are not observed on every shot and have not yet been reported on other tokamaks. Thus, it is not clear if the conditions for wake generation are somewhat special and not yet simulated or if the simulation models that are presently available lack some critical ingredients.

Simulations have seen instability of blob fronts due to interchange physics, which can cause poloidally varying fingerlike structures to appear.[5] These are well documented, but they are associated with the blob itself on the steep leading edge and are not expected to form a wake. Also well documented[5] is the fact that the tail of the blob can be unstable in simulations due to local Kelvin-Helmholtz-induced blob breakup. However, this effect is associated with strong nonlinear vorticity advection (ion polarization current) and produces a turbulent, smokelike, train. It would not be expected to result in very regular well-defined structures seen in the experimental data.

Although a definitive theoretical interpretation of the wakes is not apparent, a plausible candidate mechanism may be useful to guide further experimental tests of the mechanism and more quantitative theoretical modeling. The proposed mechanism discussed in the following is wave emission by the blob. Indeed, the limited space and time structure of the wakes seems to be due to the localized plasma perturbations from the blobs. The local increase in the density and/or temperature associated with the blobs themselves, but not directly measured in these experiments, may trigger wave emission. The mechanism for excitation of the waves is not entirely clear, but the blobs have a variable and complicated structure and motion not captured by a simple poloidal velocity, which is hard to define precisely; for example, Fig. 10 shows that the blobs do more than just move poloidally like rigid bodies. It is possible that this additional structure and motion as the blobs evolve internally and are jostled about by the surrounding turbulence is a cause for wave emission.

In the following, candidate wave estimates employ plasma parameters based on Refs. 1 and 4; similar discharges are considered in Ref. 4. We assume a factor of up to 2 uncertainty in plasma parameters and probably more on the lower end in n_e and T_e depending on how far into the SOL the wakes are observed. Gradient scale lengths are particularly uncertain. The base case parameters at the location of the wakes (in the near SOL) are taken to be $Z = 1$, $\mu = 2$ (deuterium), $B = 2.6$ kG, ($B_0 = 4.9$ kG on axis), $T_e = T_i = 15$ eV, $n_e = 1.6 \times 10^{13}$ cm^{-3}, $Z_{eff} = 2$, the density gradient scale length is taken to be $L_n = 1$ cm. For the wake, the wavelength is $\lambda_w = 3.5$ cm and $k_w = 2\pi/\lambda_w = 1.7$ cm^{-1}. Typical device geometry parameters are taken to be $R = 150$ cm (at the wake) and $L_{||} = 600$ cm, the connection length along a field line from the midplane to the target plate at a distance of 2 cm into the SOL (over a range of 1–3 cm into the SOL, a typical variation of the NSTX connection length is $L_{||} \sim 500$–750 cm).

The electron drift wave is a natural candidate for the wake structures because drift waves are ubiquitous in tokamaks and the observed velocity is in the electron direction. The characteristic fluid drift wave frequency in the plasma frame is given by

$$\omega = \frac{\omega_{*e}}{1 + k_\perp^2 \rho_s^2}, \tag{1}$$

where $\omega_{*e} = k_y c_s \rho_s / L_n$, $\rho_s = c_s/\Omega_i$, and c_s is the sound speed. Estimating $k_\perp = k_y = k_w$, where the "y" direction is poloidal (technically binormal), we find $k_\perp \rho_s = 0.37$ which is the expected order of magnitude for linear drift waves. The drift frequency estimate is $\omega = 8.8 \times 10^5\ s^{-1}$ and the corresponding phase velocity in the y direction in the plasma frame is $v_p = \omega/k_y = c_s \rho_s / L_n = 5.0$ km/s. The observed phase velocities of most of the wake structures in the lab frame are in the range of 1.5 ± 1.0 km/s. However, it is likely that the observed blobs, which move in the ion direction, are so moving because of a background $E \times B$ flow generated from the electron temperature gradient and the sheath potential. The blob velocities are estimated to be in the range of 0 to −3 km/s (i.e., in the ion direction). If this is indeed the $E \times B$ velocity of the background plasma, the net phase velocity of the drift wave in the lab frame $v_{p,lab} = v_p + v_E$ would still be in the electron direction and within a factor of 2 of the observed phase velocity of the wakes. The estimated drift-wave phase velocity is somewhat high compared to the observations but could be reduced if L_n were larger than 1 cm, which might be the case as one moves more deeply into the SOL. The drift waves would only propagate away from the blob in the electron direction; there would be no expectation of waves in the ion direction, i.e., "below" the blob in the geometry of the images, and (almost) none are observed in the GPI data.

Another wave of interest is the torsional (slow) Alfvén wave. In the edge and SOL, Alfvén waves are associated with a large gradient in the plasma beta, ($\beta = c_s^2/v_A^2$, where v_A is the Alfvén speed) sometimes characterized by the dimensionless parameter $\alpha_{mhd} = \beta/(k_{||}^2 R L_n)$. (The form usually quoted on closed flux surfaces, where $k_{||} \sim 1/qR$ is $\alpha_{mhd} \rightarrow q^2 R\beta/L_n$.) For our parameters, estimating $k_{||} = 0.003$–$0.01\ cm^{-1}$ (see below) α_{mhd} is in the range of 0.1–1.0 motivating the following more detailed estimates. Depending on regimes, several forms for the Alfvén wave dispersion relation are possible.[15,16] The collisionless fluid limit requires $k_{||} v_{te} \ll \omega$ and $\omega_\eta \ll \omega$, where $\omega_\eta = 0.51 \nu_e k_\perp^2 \delta_e^2$ and ν_e is the electron Coulomb collision frequency. In this case, in the plasma frame, the dispersion relation is

$$\omega^2 = \frac{k_{||}^2 v_A^2}{1 + k_\perp^2 \delta_e^2}, \tag{2}$$

where $k_{||}$ is the parallel wavenumber and $\delta_e = c/\omega_{pe}$ is the electron skin depth. In the collisional fluid limit, $\omega_\eta \gg \omega$, the Alfvén waves are purely damped with $\omega = -i k_{||}^2 v_A^2/\omega_\eta$. These two cases are sublimits of Eq. (24) in Ref. 16. In the kinetic limit $k_{||} v_{te} \sim \omega$, where v_{te} is the electron thermal velocity, the Alfvén waves are Landau damped, but for $k_{||} v_{te} \gg \omega$, where the electrons have an adiabatic response ($\delta n/n \sim e\delta\Phi/T_e$), there is again propagation with

$$\omega^2 = k_{||}^2 v_A^2 \left(1 + k_\perp^2 \rho_s^2\right). \tag{3}$$

This wave is the kinetic Alfvén wave discussed in Ref. 15.

For purposes of estimation, we assume that the Alfvén wave is a maximum at the outboard midplane and approximately zero somewhere between the X-point (where magnetic shear and dissipation begin to set in) and the location of the divertor target. As there are no available experimental data on the parallel structure, this assumption is speculative but theoretically motivated by field-line bending effects from blobs due to Alfvén wave physics.[17] The corresponding midplane-node distance along a field line is roughly in the range R (for a spherical torus with its large outboard midplane B-field pitch) to the target connection length $L_{||}$, i.e., 150–600 cm. This midplane-node distance is then a quarter wavelength and we estimate $k_{||}$ to be in the range of $\pi/(2\,L_{||})$ to $\pi/(2\,R)$, i.e., $k_{||} = 0.003$–$0.01\ cm^{-1}$. Using the other base case parameters, we have $v_{te}/v_A = 1.6$. Thus, the Alfvén wave is marginally in the kinetic limit of Eq. (3) and we find $\omega = \pm(3.4\text{ to }11) \times 10^5\ s^{-1}$, while the poloidal phase velocity in the plasma frame is $v_p = \omega/k_y = \pm(1.9\text{ to }6.4)$ km/s. In the lab frame, we would have $v_{p,lab} = v_p + v_E$ where, as discussed for the drift wave, presumably $v_E < 0$. Alfvén waves excited by the blob would be expected in both the electron and ion directions, although their phase velocities in the lab frame would be asymmetric. The simple fact of both electron and ion-directed Alfvén wakes (in the plasma frame) may be inconsistent with the observations. However, in addition to pure Alfvén waves, there is the possibility of drift-Alfvén wave coupling.

Both the electron drift wave and the Alfvén wave have wave parameters that are roughly similar to each other and to the observations. In this situation, the drift and Alfvén waves can interact near their mode crossing resulting in drift-Alfvén modes.[18,19] Drift-Alfvén modes would preferentially propagate in the electron direction, as observed. Mode crossing occurs approximately when $\omega_{*e} \equiv k_y v_{*e} = k_{||} v_A$. k_y satisfying this condition is of the order of magnitude of the observed wake value of k_w. We speculate that this is one plausible mechanism for explaining the fact that a single k_w seems to be seen in the wake of a given shot, rather than broadband turbulence that might be expected from the drift wave alone.

Since the wakes are only observed in the SOL, it is also reasonable to consider the possibility of SOL-specific instabilities. One such mode is the sheath-connected "conducting wall" mode.[20] This mode is driven by the SOL electron temperature gradient acting in combination with the associated SOL radial electric field arising from the sheath potential $\Phi \sim 3T_e$. In order of magnitude, the conducting wall mode has a frequency $\omega \sim \omega_{*eT}$, the electron temperature gradient drift frequency, which because of the sheath physics is also of order $k_y v_E$. Parameter estimates are thus similar to those of the electron drift wave. The conducting wall mode can be localized near the target plate, but that regime would not be relevant here. It can extend along the field line, but the available analyses assume sheaths on both ends of the field line, a situation which is probably not strictly relevant to the single null discharges considered in this paper. A definitive statement about the relevance of this mode would require an additional study.

In the experiments, wakes are only observed in some of the cases. In the wave paradigm, wakes might not be excited in all situations for several reasons: if the blobs emit frequencies larger than $\omega_{*e}/2$, no drift waves could be excited according to Eq. (1); if the plasma is too collisional ($\omega_\eta > \omega$) or in the regime $\omega \sim k_{||} v_{te}$, Alfvén waves would be strongly damped. The linear wave theory discussed here is not sufficient to explain the variation of wake velocity and wavelength with wake amplitude shown in Figs. 9(b) and 9(c). However, the wave paradigm is not inconsistent with Fig. 9(d): for a constant blob emission frequency, we would expect $v_w \propto \lambda_w$, where v_w is the wake phase

velocity in the plasma frame. Although Fig. 9(d) shows the wake velocity in the lab frame, a general increase in the wavelength would still be expected.

Thus, although not definitive, there is some evidence that the wakes may be waves excited by the blobs. Candidate waves include drift waves and drift-Alfvén waves. These waves share some features such as wavenumber and phase velocity which are roughly similar to the observations.

E. Future directions

The most important thing needed for an improved study of blob wakes in NSTX is a fully automated code to identify wakes and blobs in the GPI camera data. At present, the wake characteristics are not well defined enough to construct a search algorithm to identify wakes and to quantify their relationship with blobs. This algorithm may benefit from sophisticated "machine learning" techniques, since the wakes identified by eye have significantly variable space/time patterns, as illustrated in Figs. 2, 4, 6, 7, and 8.

Specific aspects of the present wake analysis which should be improved are identification of the wake velocity (presently limited to $\geq$0.3 km/s in the electron diamagnetic direction), evaluation of the wake wavelength spectrum (presently limited to one average wavelength), and better estimates of the wake amplitude (presently averaged over a space-time segment). The wake analysis should extend over the whole edge and SOL and not be restricted to a single chosen radius, as done at present. The time-dependent wake formation process should be analyzed in detail; for example, perhaps the wakes are triggered by some specific blob shape or tilt or by radial variations in the blob velocity profile.

Hardware improvents could also aid the future study of blob wakes, since the observed wavelengths down to $\lambda_{pol} \sim 2$ cm are near the ~0.5 cm optical resolution limit of the present NSTX GPI diagnostic. A zoom lens system with a resolution of ~0.1 cm has already been installed for NSTX-U. The angular misalignment of the GPI view with the local B field line is also a limitation, but this might be optimized on a shot-to-shot basis using remotely controlled optics. The direct measurement of local blob density and temperature would greatly aid the theoretical modeling and might be obtained with a dedicated edge Thomson scattering system.

Existing numerical simulations of edge turbulence in NSTX have found a variety of unstable modes in the pedestal region[12,21] but did not cover the SOL region. Seeded blob simulations of SOL turbulence in NSTX[22] have not yet seen wakes, but the parameter space could be explored further. These simulations are needed to clarify whether the observed wake modulations in GPI are due to electron density or temperature fluctuations. The possible effects of the GPI neutral gas on wake formation should also be considered.

Finally, the present paper focused on wakes in a small set of high-power H-mode plasmas, but there are similar small-scale structures in many other shots in the NSTX GPI 2010 database.[14] A comprehensive search for wakes and other small-scale structures could be made once an automated algorithm is developed.

F. Conclusions

Transient small-scale structures were identified in the wake of blobs moving poloidally through the SOL of high-powered H-mode plasmas in NSTX. The observed structures as seen using gas puff imaging (GPI) had a poloidal wavelength in the range of $\lambda_{pol} = 3.5 \pm 0.7$ cm, which is significantly smaller than a typical blob scale of $L_{pol} \sim 12$ cm, and had a wake poloidal velocity of $V_{pol} = 1.5 \pm 1.0$ km/s in the electron diamagnetic direction, which is opposite to the typical blob velocity. These wakes were localized radially within 0–4 cm outside the separatrix and occurred within ~50 μs after the passage of a blob through the GPI field of view. The clearest wakes were seen when the GPI view was well aligned with the local B field line, as expected for these small-scale structures given the diagnostic geometry.

Although a definitive theoretical interpretation of the wakes cannot be given at this time, it is argued that the observed wakes may be waves that are excited by the blobs. Candidate waves include drift waves and/or drift-Alfvén waves. These waves share some features such as wavenumber and phase velocity which are roughly similar to the observations. It is hoped that the wave emission interpretation may be useful to guide further experimental tests of the mechanism and more quantitative theoretical modeling.

SUPPLEMENTARY MATERIAL

See the supplementary material for a video of the raw GPI data in Fig. 7.

ACKNOWLEDGMENTS

We thank W. Guttenfelder and D. R. Smith for discussions on this topic, R. J. Maqueda and W. Davis for long-term collaboration on the NSTX GPI diagnostic, B. LeBlanc for the Thomson scattering data, and the NSTX/NSTX-Upgrade Team for the support of this work. This material is based upon the work supported by the USDOE Contract No. DE-AC02 09CH11466 and the Office of Fusion Energy Sciences Award No. DE-FG02-02ER54678. Portions of this research were performed under the auspices of the U.S. DOE by the Lawrence Livermore National Laboratory under Contract No. DE-AC52-07NA27344. The digital data for this paper can be found in http://arks.princeton.edu/ark:/88435/dsp018p58pg29j.

APPENDIX: ANALYSIS OF BLOB WAKES

Blob wakes were identified by eye using plots such as shown in Fig. 7, in which the spatially smoothed and normalized GPI signal is plotted as a function of the poloidal location in one column of the 2D GPI frame vs time. The wake analysis was discussed in Sec. II F, but in this appendix, we describe the analysis steps and limitations of the algorithm in more detail for a specific data segment, namely, segment #7 from shot #139 048, previously shown in Figs. 7(a) and 8(a).

(a) The first step is to identify by eye a segment of GPI data with a clearly visible wake pattern, as discussed in Sec. II E, and shown for this example in Fig. 11(a). Each such segment extends vertically 15 cm in the poloidal direction (40 rows of the original GPI image) and 50 μs horizontally in time (20 GPI camera frames). These segments were rebinned and linearly interpolated into a 120 × 120 pixel format for visual clarity, as for Fig. 11(a).

(b) This 120 × 120 segment is then rotated counterclockwise about its center point in 1° increments to find the wake alignment angle in this space-vs-time plot, using the method described in (c)

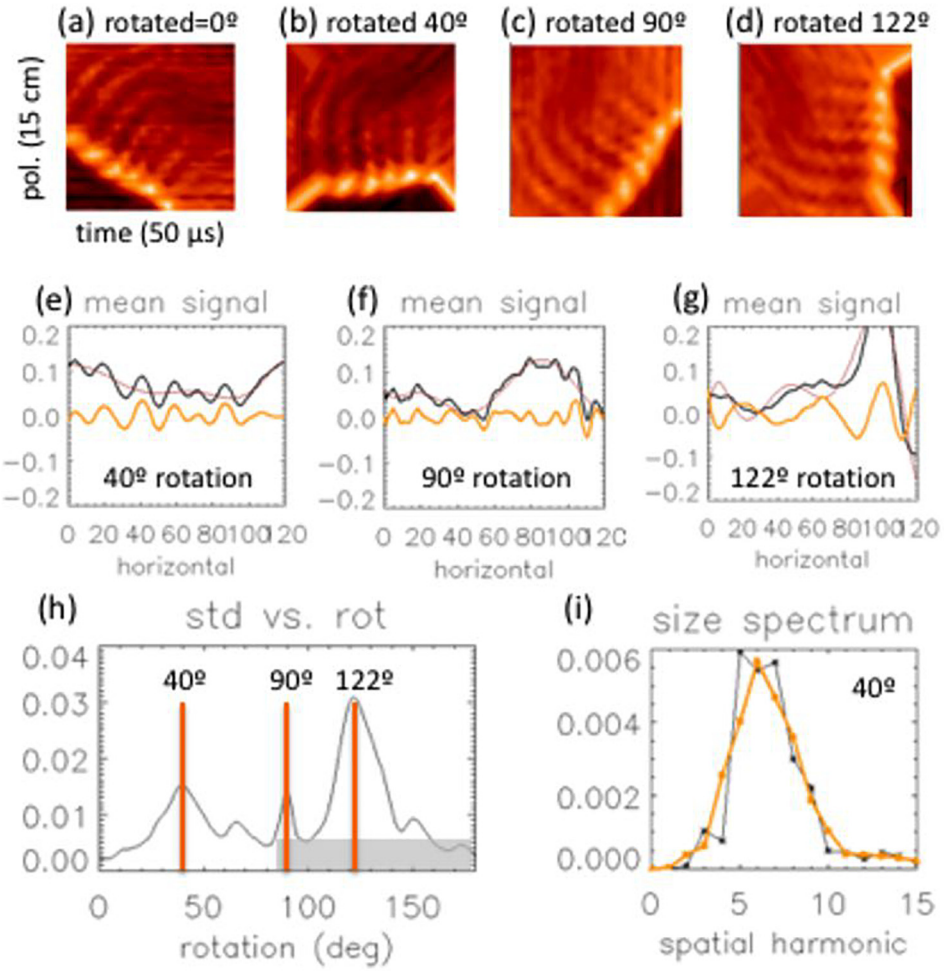

FIG. 11. Details of the wake analysis method as applied to a single data segment (see the Appendix). (a) is a GPI data segment with a clear blob wake, and (b) is the image rotated 40° around its center so that the wake is aligned vertically. (c) and (d) are two other rotation angles of interest. In (e), the dark black line is the mean signal vs horizontal column in (b) for the 40° rotation, the thin red line a polynomial fit to that, and the orange line is the difference between the two, which is the wake amplitude vs this horizontal direction. (f) and (g) are the corresponding plots for (c) and (d). (h) is the standard deviation of the wake amplitude vs rotation angle showing the wake angle peak at 40° and a spurious peak near 90° and 122° (the shaded region is not used in the final analysis). Part (i) shows the spectrum of spatial harmonics for the segment rotated by 40°.

below. Before rotation, the segment is smoothed over 5/120 rows in the poloidal (vertical) direction (i.e., 0.3 cm) to reduce systematic pixel-to-pixel variations in the raw data [recall that each row in Fig. 11(a) corresponds to a single vertical column in the 2D GPI image]. For the segment in Fig. 11(a), the optimum rotation angle for vertically aligning the wakes is at $\theta = 40°$, and the rotated segment at this angle is shown in Fig. 11(b). This angle is then used to determine the wake poloidal velocity, as described in Sec. II F; for example, a rotation angle of 45° corresponds to a wake velocity of 15 cm/50 μs = 3 km/s in the upward (electron diamagnetic drift) direction. The segment rotation is done in IDL using "rot/interp" and so does an interpolation at the corners of the segments. Two other rotated segments of interest for this analysis are at $\theta = 90°$ and 122°, as shown in Figs. 11(c) and 11(d), respectively, and discussed in (h).

(c) For each 1° rotation step, the mean value in the vertical direction of the rotated segment vs horizontal column number is determined, e.g., as the black line in Fig. 11(e) for the 40° rotation of Fig. 11(b). This line is then fit by a 7th order polynomial, as shown by the thin red line, to remove the slowly varying spatial components, which are not part of the small-scale wake. The difference between the black and thin red curves is shown by the thick orange curve in Fig. 11(e). This is the normalized small-scale wake amplitude vs horizontal direction at a rotation angle of $\theta = 40°$. Similar plots for the other two rotation angles are shown in Figs. 11(f) and 11(g).

(d) The wake rotation angle is then determined as the angle at which the standard deviation in the wake amplitude vs the horizontal direction of the rotated image has a local maximum, as illustrated in Fig. 11(h). In this case, a rotation of $\theta = 40°$ best corresponds to vertically aligned wakes as seen by eye in Fig. 11(b). However, we find that there are also sometimes "spurious" local peaks in the wake amplitude vs rotation angle within the angle range $\theta = 85°$–180°, such as the peaks at $\theta = 90°$ and 122° in Fig. 11(h), which are discussed in paragraph (h).

(e) The wake velocity is estimated from the wake rotation angle as $V_{pol} = (3/\tan\theta)$ km/s, based on space and timescales described in paragraph (b). Due to the present constraint on the rotation angles of $\theta \leq 85°$, as indicated by the shaded region in Fig. 11(h), these wake speeds are constrained to $V_{pol} \geq 0.3$ km/s in the electron diamagnetic direction. However, this includes almost all the clear wakes, as illustrated in Fig. 7.

(f) The wake amplitude is then estimated as the standard deviation of the wake fluctuations such as shown in orange in Fig. 11(e) over the 120 columns in the horizontal direction of the rotated image. The wake amplitude at $\theta = 40°$ in this case is A = 0.015.

Since these wake amplitudes are averaged over the vertical extent of the rotated segments such as (b), they underestimate the maximum wake amplitude if the wake structure does not fill the segment area, as is usually the case (see Fig. 8). This wake amplitude is therefore only an approximate measure of the relative strength of the wake.

(g) The wavelength of the wake in the poloidal direction λ_{pol} is estimated using the spatial Fourier spectrum of the wake amplitude in the horizontal direction of the rotated segment, as shown by the black curve in Fig. 11(i). Since there are normally several harmonics in this spectrum, only the peak of the spectrum after smoothing over 3 harmonics is used, as shown in orange in Fig. 11(i). In this case, the peak is at the $H = 6$ spatial harmonic number in the horizontal direction of Fig. 11(e). The poloidal wavelength of this wake in the vertical direction of Fig. 11(a) is then estimated as $\lambda_{pol} = 15.0\,\text{cm}/(H^{*}\sin\,\theta) = 3.9\,\text{cm}$. The wake wavelength in this analysis is correlated with the wake velocity by $V_{pol} = 0.2\,\lambda_{pol}\,(H\cos\theta)$, as illustrated in Fig. 9(d).

(h) Returning to the spurious peaks at $\theta = 90°$ and 122° in Fig. 11(h), the peak at 90° is caused by residual pixel-to-pixel variations in the columns of the raw GPI camera data, which can be faintly seen as vertical lines in the segment rotated by 90° in Fig. 11(c). These were incompletely removed by averaging over 5/120 rows as described in paragraph (b) but could not be further suppressed since this would then begin to dampen the wake structures. Within the unconstrained rotation range of $\theta = 0°$–180°, 54% of the segments with small but visible wakes (W1) had such spurious peaks at exactly $\theta = 90°$ and 17% of the clear wake segments (W2 and W3) had spurious peaks at exactly $\theta = 90°$, which motivates the constraint of $\theta \leq 85°$ used in the analysis of clear wakes for Fig. 10. The spurious peak at 122° in Fig. 11(h) is caused by the edges of the blob structures and not the wakes, as illustrated by the bright vertical edge at the right in Figs. 11(d) and 11(g). These edges move in the opposite direction to the wakes, as shown in Fig. 6(b), and were not completely removed by the spatial high-pass filtering described in Fig. 3. Within the unconstrained rotation range of $\theta = 0°$–180°, about 36% of the segments with small but visible wakes (W1) had spurious wake peaks within $\theta = 95°$–180° and about 48% of the clear wake segments (W2 and W3) had spurious wake peaks in this range. Since very few wakes were observed by eye to move in the blob (ion diamagnetic drift) direction, this motivates the exclusion of local peaks in the range of $\theta = 85°$–180° for the determination of the clear wake velocities in Fig. 10.

This wake analysis process was successfully tested using coherent sine waves of various wavelengths and angles in place of the GPI data in Fig. 7. However, the results for real GPI data should be considered only an approximation, due to the limitations and approximations mentioned above and in Sec. II F. For example, the analysis was limited to a wavelength range $\lambda_{pol} \sim 2$–6 cm by the GPI spatial resolution and the high-pass filtering and to the poloidal velocity range $V_{pol} > 0.3$ km/s in the electron diamagnetic direction by spurious peaks at $\theta \geq 85°$ in plots like those in Fig. 11(h). These limitations can eventually be overcome by improved diagnostic and analysis methods, as discussed in Sec. III E.

REFERENCES

[1]A. Diallo, J. Dominski, K. Barada, M. Knolker, G. J. Kramer, and G. McKee, Phys. Rev. Lett. **121**, 235001 (2018).
[2]S. I. Krasheninnikov, Phys. Lett. A **283**, 368 (2001).
[3]J. A. Boedo, D. Rudakov, R. Moyer, S. Krasheninnikov, D. Whyte, G. McKee, G. Tynan, M. Schaffer, P. Stangeby, P. West, S. Allen, T. Evans, R. Fonck, E. Hollmann, A. Leonard, A. Mahdavi, G. Porter, M. Tillack, and G. Antar, Phys. Plasmas **8**, 4826 (2001).
[4]S. J. Zweben, J. R. Myra, W. M. Davis, D. A. D'Ippolito, T. K. Gray, S. M. Kaye, B. P. LeBlanc, R. J. Maqueda, D. A. Russell, D. P. Stotler, and NSTX Team, Plasma Phys. Controlled Fusion **58**, 044007 (2016).
[5]D. A. D'Ippolito, J. R. Myra, and S. J. Zweben, Phys. Plasmas **18**, 060501 (2011).
[6]F. Militello, P. Tamain, W. Fundamenski, A. Kirk, V. Naulin, A. H. Nielsen, and MAST Team, Plasma Phys. Controlled Fusion **55**, 025005 (2013).
[7]D. Carralero, S. Artene, M. Bernert, G. Birkenmeier, M. Faitsch, P. Manz, P. de Marne, U. Stroth, M. Wischmeier, E. Wolfrum, ASDEX Upgrade Team, and EURO-Fusion MST1 Team, Nucl. Fusion **58**, 096015 (2018).
[8]C. K. Tsui, J. A. Boedo, J. R. Myra, B. Duval, B. Labit, C. Theiler, N. Vianello, W. A. J. Vijvers, H. Reimerdes, S. Coda, O. Fevrier, J. R. Harrison, J. Horacek, B. Lipschultz, R. Maurizio, F. Nespoli, U. Sheikh, K. Verhaegh, N. Walkden, TCV Team, and EUROfusion MST1 Team, Phys. Plasmas **25**, 072506 (2018).
[9]G. Fuchert, G. Birkenmeier, M. Ramisch, and U. Stroth, Plasma Phys. Controlled Fusion **58**, 054005 (2016).
[10]S. J. Zweben, D. P. Stotler, F. Scotti, and J. R. Myra, Phys. Plasmas **24**, 102509 (2017).
[11]S. J. Zweben, J. L. Terry, D. P. Stotler, and R. J. Maqueda, Rev. Sci. Instrum. **88**, 041101 (2017).
[12]A. Diallo, G. J. Kramer, D. R. Smith, R. Maingi, R. E. Bell, W. Guttenfelder, B. P. LeBlanc, M. Podestà, G. J. McKee, and R. Fonck, Phys. Plasmas **20**, 012505 (2013).
[13]See https://w3.pppl.gov/~szweben/NSTX2013/NSTX2013.html for NSTX database.
[14]See https://w3.pppl.gov/~szweben/NSTX%20wakes/ for NSTX wake movies.
[15]R. L. Lysak, Phys. Plasmas **15**, 062901 (2008).
[16]J. R. Myra, D. A. D'Ippolito, X. Q. Xu, and R. H. Cohen, Phys. Plasmas **7**, 4622 (2000).
[17]S. I. Krasheninnikov, D. D. Ryutov, and G. Yu, J. Plasma Fusion Res. SERIES **6**, 139 (2004); available at http://www.jspf.or.jp/JPFRS/PDF/Vol6/jpfrs2004_06-139.pdf.
[18]P. N. Guzdar, L. Chen, P. K. Kaw, and C. Oberman, Phys. Rev. Lett. **40**, 1566 (1978).
[19]J. R. Myra, D. A. D'Ippolito, and X. Q. Xu, Phys. Plasmas **9**, 1637 (2002).
[20]H. Berk, D. D. Ryutov, and Yu. A. Tsidulko, JETP Lett. **52**, 23 (1990).
[21]M. Coury, W. Guttenfelder, D. R. Mikkelsen, J. M. Canik, G. P. Canal, A. Diallo, S. Kaye, G. J. Kramer, R. Maingi, and NSTX-U Team, Phys. Plasmas **23**, 062520 (2016).
[22]J. R. Myra, W. M. Davis, D. A. D'Ippolito, B. LaBombard, D. A. Russell, J. L. Terry, and S. J. Zweben, Nucl. Fusion **53**, 073013 (2013).